EXPERIMENTAL INVESTIGATION OF THE HYDRODYNAMIC FORCES ON THE SHROUD OF A CENTRIFUGAL PUMP IMPELLER

Thesis by

Fei Zhuang

Division of Engineering and Applied Science

In Partial Fulfillment of the Requirements

for the

Engineer's Degree

California Institute of Technology

Pasadena, California

1989

(Submitted May 26, 1989)

ACKNOWLEDGEMENTS

I would like to express my gratitude to Professor A. J. Acosta for his guidance and advice during the course of this research. I would also like to thank Professors C. E. Brennen and T. K. Caughey for their continued interest in this research.

I would like to thank George Lundgren and his team for the machining of the test apparatus. I am also thankful to Mike Gerfen, who assisted the initial installation of the apparatus.

The assistance provided by Ron Franz, Norbert Arndt, Faress Rahman, and Adiel Guinzburg is appreciated. I also want to thank the others not mentioned here for their various contributions to this research.

For their help in preparing the thesis, I would like to thank Dana Young and Cecilia Lin. The help of Jackie Beard with the administrative tasks is also appreciated.

I gratefully acknowledge the Byron-Jackson Pumps Division for providing a fellowship that supported my graduate studies. This research was supported by NASA George C. Marshall Space Flight Center under contract NAS8-33108 and grant NAG8-118.

Finally, sincere thanks go to my parents and my sister for the understanding and the encouragement they have given to me. I dedicate this thesis to my wife, Ying Sun, whose support, caring and inspiration are greatly appreciated.

ABSTRACT

Fluid-induced forces acting on a rotating impeller are known to cause rotordynamic problems in turbomachines. The forces generated by leakage flow along the front shroud surface of a centrifugal turbomachine impeller play an important role among these fluid-induced forces. The present research was aimed to gain a better understanding of these shroud forces. An experimental apparatus was designed and constructed to simulate the impeller shroud leakage flow. Hydrodynamic forces, steady and unsteady pressure distributions on the rotating shroud were measured as functions of eccentricity, width of shroud clearance, face seal clearance and shaft rotating speed. The forces measured from the dynamometer and manometers agreed well. The hydrodynamic force matrices were found skew-symmetric and statically unstable. This is qualitatively similar to the result of previous hydrodynamic volute force measurements. Nondimensionalized normal and tangential forces decrease slightly as Reynolds number increases. As the width of the shroud clearance decreases and/or the eccentricity increases, the hydrodynamic forces increase nonlinearly. There was some evidence found that increased front seal clearance could reduce the radial shroud forces and the relative magnitude of the destabilizing tangential force. Subharmonic pressure fluctuations were also observed which may affect adversely the behavior of the rotor system.

TABLE OF CONTENTS

NOMENCLATURE

$[A]$	hydrodynamic force matrix, non dimensionalized by $\frac{1}{2}\rho u_2^2 \varepsilon L/R_2$
$[B]$	calibration matrix for the rotating dynamometer
$[C]$	hydrodynamic damping matrix
c_i	magnitude of i^{th} Fourier coefficient
$\bar{c}_p$	static pressure coefficient, $\bar{c}_p = \frac{p-p_1}{\frac{1}{2}\rho u_2^2}$
$\tilde{c}_p$	unsteady pressure coefficient
$\tilde{c}_{p,av}$	ensemble averaged unsteady pressure coefficient
F	lateral force on the rotating shroud
F_o	values of F if the rotating shroud was located at the origin of the stationary shroud frame (stationary shroud center)
F_{ox}, F_{oy}	values of F_x and F_y if the rotating shroud was located at the stationary shroud center, non-dimensionalized by $\frac{1}{2}\rho u_2^2 \varepsilon L$
F_1, F_2	components of the instantaneous lateral force on the rotating shroud in the rotating dynamometer reference frame
F_n, F_t	components of the lateral force on the rotating shroud which are normal and tangential to the whirl orbit, averaged over the orbit, non-dimensionalized by $\frac{1}{2}\rho u_2^2 \varepsilon L$
F_x, F_y	components of the lateral force on the rotating shroud in the stationary laboratory frame, i.e., in horizontal and vertical directions of the laboratory non-dimensionalized by $\frac{1}{2}\rho u_2^2 \varepsilon L$

H	averaged width of the clearance between the rotating shroud surface and stationary shroud surface
$[K]$	hydrodynamic stiffness matrix
L	projected length of the leakage path along meridional direction of the rotating shroud surface
m	mass of the rotating shroud and the spindle
$[M]$	hydrodynamic mass matrix
$\tilde{p}$	unsteady pressure
p_1, p_{t1}	shroud flow discharge static, total pressure
p_2, p_{t2}	shroud flow inlet static, total pressure
Q	flow rate
R_o	the inner radius of the stationary shroud at the center of the holes for clearance measurement
R_e	Reynolds number, $\frac{u_2 R_2}{\nu}$
R_2	rotating shroud inlet radius
s	area of the rotating shroud surface
t	time
u_2	tip speed at the rotating shroud inlet, ωR_2
X	displacement vector of the rotating shroud from the stationary shroud center
x, y	components of X in rectangular directions
α	angular position on the surface of the rotating shroud

δ	front face seal clearance
δ_H	the change of the clearance H
ε	distance between the centers of the rotating shroud and stationary shroud
ρ	density of water
ζ	angular location of the rotating shroud center
ω	radian frequency of the shaft rotation
Ω	radian frequency of the whirl motion
ϕ	flow coefficient, $\frac{Q}{2\pi H R_2 u_2}$
ψ	total head coefficient, $\frac{p_{t2}-p_{t1}}{\rho u_2^2}$
θ	angular position on the surface of the stationary shroud
φ	phase angle of the shroud lateral hydrodynamic force, $\varphi = tg^{-1}\frac{F_t}{F_n}$
φ_o	phase angle of the average shroud lateral hydrodynamic force, $\varphi_o = tg^{-1}\frac{F_{oy}}{F_{ox}}$

Subscripts:

av	ensemble averaged
max	maximum

Superscripts:

$-$	steady, time mean
$\sim$	unsteady
$*$	normalized

List of Figures

List of Tables

Chapter 1

INTRODUCTION

1.1. Description of the Problem

In recent years, rotordynamic instability problems have received more and more attention among designers, manufacturers and operators of high performance turbomachines. In space application, propellant pumps tend to have very high operating speeds and relatively smaller size and weight. But at these higher speeds, the forces acting on the impeller may cause severe, unexpected vibration problems such as rotor whirling, large bearing loads, even structure failure of the pump. So it is necessary to have a clearer understanding of what causes the forces on the impeller and what can be done to minimize their impact.

There are two categories of forces acting on the impeller. One comes from the mechanical system, such as rotor mass unbalance, etc., the other one comes from the working fluid, called fluid-induced forces. Several sources have been identified as contributing to the fluid-induced forces. One area that has received a lot of attention is the force generated by fluid in the annular seals separating the high pressure discharge of the pump from the relatively low pressure inlet (Childs, 1983). The second one is the hydrodynamic force that arises from the interaction between the impeller and its accompanying volute (Jery, et al. 1985, Franz, et al. 1987). A third area is the hydrodynamic force caused by fluid trapped between the front shroud of the rotating impeller and the stationary pump casing; that is, the forces generated by the shroud leakage flow, and disk friction. The present thesis focuses on these shroud forces.

1.2. Survey of Current Knowledge

The primary emphasis of this study was to investigate the radial forces that result from the hydrodynamic interaction between the front shroud of the impeller and the casing. Figure 1.1 is a schematic of a centrifugal pump impeller undergoing whirl and Figure 1.2 indicates the forces acting upon a whirling impeller. It is customary in rotordynamic analysis to represent the radial forces by the expression

$$F(t) = F_o + [A]X(t) \tag{1.1}$$

or

$$\begin{Bmatrix} F_x(t) \\ F_y(t) \end{Bmatrix} = \begin{Bmatrix} F_{ox} \\ F_{oy} \end{Bmatrix} + \begin{bmatrix} A_{xx} & A_{xy} \\ A_{yx} & A_{yy} \end{bmatrix} \begin{Bmatrix} x(t) \\ y(t) \end{Bmatrix} \tag{1.2}$$

i.e., the radial force F can be considered as the sum of two forces: A steady force F_o, which the impeller would experience if located at the volute center, arising from asymmetries in the flow around the impeller, and an unsteady force due to the eccentric motion of the impeller, represented by a hydrodynamic force matrix $[A]$; $X(t)$ is the displacement vector of the impeller from the volute center. The hydrodynamic force matrix $[A]$ will in general be a function of the frequency of lateral vibration, impeller-casing geometry, and the operation condition of the turbomachine. Frequently, the unsteady force is expanded in terms of the time derivatives of $X(t)$ with the coefficient matrices being the stiffness, damping and mass matrices.

$$F(t) = F_o - [K]X(t) - [C]\dot{X}(t) - [M]\ddot{X}(t) \tag{1.3}$$

Clearly, if the whirl speed is equal to or very near zero, $[K]$ could be replaced by minus $[A]$ or vice-versa. In the rest of this thesis, we use $[A]$ instead of $[K]$ to present data obtained in no-whirl or very slow whirl motions measurements. The unsteady force can be resolved into components normal to and tangential to the whirl motion. The normal force is perpendicular to the whirl motion, directed radially outward when positive. The tangential force is positive when in the direction of shaft rotation. A positive normal force tends to increase the displacement of the impeller. More importantly, when the tangential force is in the same direction as the whirl velocity, it encourages the whirl motion and is thus destabilizing.

In the next part of this section, some past experimental and theoretical investigations of these hydrodynamic shroud forces will be reviewed.

Before considering the shroud forces, it is worthwhile to review some experimental results about the total hydrodynamic forces acting on the impeller. Hergt and Krieger (1969-1970) measured the force on a centrifugal impeller centered and at various eccentric locations in a vaned diffuser. The measured force was directed radially outward with a small tangential component. Kanki, et al. (1981) used strain gauges on the shaft neck to measure the force of a centrifugal impeller in a double volute and in a vaned diffuser. The impeller was positioned centered and also off-center from the casing centerline. The hydrodynamic force acted in the general direction of the impeller displacement. However, the mea-

surements above were not presented in terms of a force matrix.

Recently, some measurements of the unsteady force matrix have been made by Bolleter, et. al. (1987) from Sulzer Brothers, Ltd., Ohashi and Shoji (1987) from the University of Tokyo, and the researchers at the California Institute of Technology. Brennen, Acosta and Caughey (1980) developed a test program at the California Institute of Technology. Chamieh (1983) and Chamieh, et al. (1985) used a stationary external balance to measure the hydrodynamic stiffness of a centrifugal impeller. Using a rotating internal balance, mounted between the impeller and the drive shaft, Jery, et al. (1985) and Jery (1987) measured the forces on a centrifugal impeller whirling in a circular orbit inside various volutes. Their main experimental results could be summarized as follows: the part of the steady impeller force due to impeller displacement results in a generalized hydrodynamic stiffness matrix which is statically unstable. The direct stiffness terms were equal in magnitude and had the same positive sign, resulting in a radially outward fluid force. The cross-coupled stiffness elements were equal in magnitude and their opposite signs were such as to produce a tangential fluid force encouraging forward whirl motion of the impeller. As for unsteady average normal and tangential forces: (a) the normal force is positive for almost all values of the reduced frequency; (b) in the region of positive reduced whirl ratio between 0.0 and 0.4, the tangential force is destabilizing. The Caltech and Sulzer test programs use a radial face seal to minimize or eliminate the forces which would normally be developed by the wear-ring seals. So the measured hydrodynamic impeller forces here are mainly the combination of impeller-volute

and impeller-shroud interactions.

Adkins (1986) and Adkins and Brennen (1988) observed that pressure distribution around the front shroud of an impeller, designated Impeller X, had a significant contribution to the hydrodynamic stiffness, given approximately by

$$[A] = \begin{bmatrix} 1.6 & -0.3 \\ 0.3 & 1.6 \end{bmatrix}$$

When compared with Chamieh's (1983) direct measurements of the total hydrodynamic stiffness on the same impeller (front shroud plus volute), given approximately by

$$[A] = \begin{bmatrix} 2.0 & -0.9 \\ 0.9 & 2.0 \end{bmatrix}$$

it is seen that the pressure forces acting on the front shroud of the impeller could have a major influence on the hydrodynamic force perturbations acting on an eccentrically positioned impeller, even though Adkins measurement was made for a rather large annular gap. Adkins also reported measurements taken with the annular region surrounding the shroud exposed to the housing reservoir. This data was compared with measurements taken without the enlarged annular region and with a two-dimensional model of the impeller, Impeller Z, Franz and Arndt (1986) and Franz, et al. (1987), demonstrating that the large shroud clearances reduce the magnitude of the rotordynamic forces for reverse whirl and for the region of destabilizing forward whirl. Bolleter et al. (1987), who had a smaller gap between the impeller shroud and the casing, measured much larger

forces. Since most real centrifugal pumps have small clearances along shroud leakage flow region, these shroud forces definitely deserve more attention.

A bulk-flow model of the leakage path between an impeller shroud and a pump casing has been derived by Childs (1987). Rotordynamic coefficient predictions from his analysis are in reasonable agreement with test results from Bolleter, et al. (1985), for the direct damping and cross-coupled stiffness coefficients. The model also predicts a resonance phenomenon of the fluid system at inlet tangential velocities higher than approximately half of the impeller tip speed. The significance of this "resonance" remains undetermined experimentally. However, in this model, the clearance between the impeller shroud and pump casing is assumed to be circumferentially symmetric, and the "bulk-flow" nature of the analysis restricts its applicability to impellers having fairly small clearances between the impeller shroud and casing.

1.3. Scope of the Present Research

The present investigation was designed to measure forces and the steady and dynamic pressure distributions on the surface of a rotating shroud eccentrically located within a stationary housing with a small clearance between them. An experimental apparatus was designed to simulate the shroud leakage flow in a centrifugal pump. The objective of this research was to provide a clearer picture of the fluid-induced shroud forces and their relations with instability problems of high performance turbomachines. On the other hand, in finding the fluid mechanical origins of these shroud forces, the basic principles of fluid mechanics applied in this region could be better understood.

More specifically, as the first step of this shroud force experiment, it was decided to measure the forces and pressure distributions on the rotating shroud surface under the conditions of various width of clearances, eccentricities, face seal clearances, and the shaft rotating speeds. Tests for various whirl motions and flow rates will not be included in the present experiment.

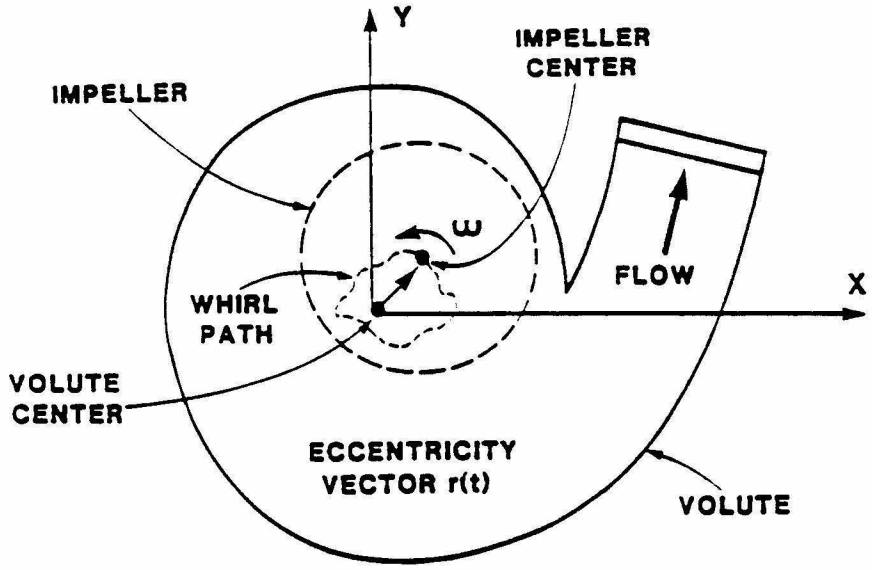

Fig. 1.1 Schematic of a centrifugal pump with a whirling impeller.

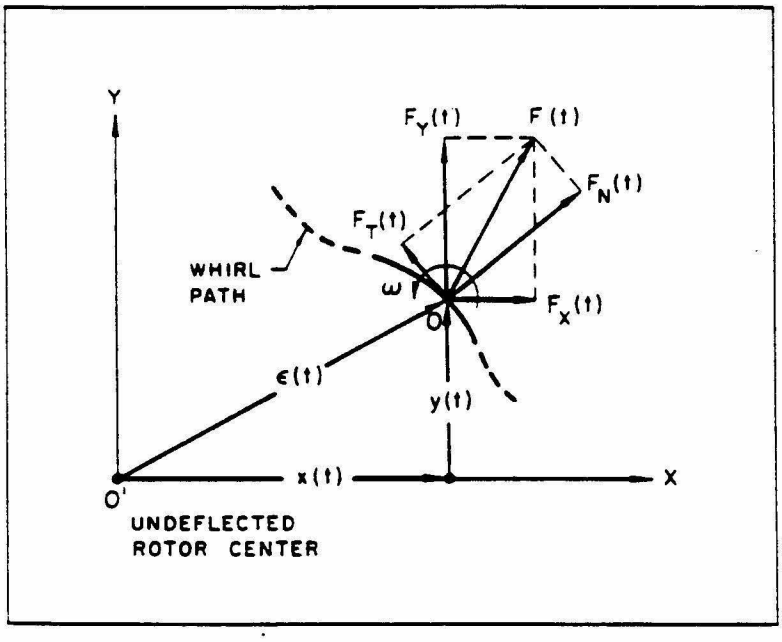

Fig. 1.2 Diagram of the forces acting on a whirling impeller in the plane of vibration.

Chapter 2

DESCRIPTION OF THE EXPERIMENTAL FACILITY AND INSTRUMENTATION

The Rotor Force Test Facility (RFTF) at the California Institute of Technology was used in the present investigation of shroud forces. This facility has been described in detail by Ng (1976), Braisted (1979), Chamieh (1983), Jery (1987), Arndt (1988) and Franz (1989).

In Figure 2.1, an overhead view of the RFTF that identifies its most important components is presented. The shroud force and pressure measurements were made in the centrifugal pump test section of the closed recirculating loop. The shroud force apparatus located in this section circulates leakage flow in the loop but was not measured since it was too small to be measured by the existing turbine flow meter. The overall system pressure was regulated by the air cell in the isolation portion of the loop. A heat exchanger permitted maintaining a constant water temperature during the experiments. The rotating shroud (see chapter 3), mounted on the drive shaft, was driven by the main motor (20 hp d.c.). By using a 2:1 step-up gear box, shaft speeds up to 3500 rpm could be obtained. The whirl motor was not used for the present work. Using optical encoders to provide feedback, each motor was closed-loop controlled to be synchronized with data acquistion. A magnetic pick-up transducer, in conjunction with an HP5302 universal counter, was used to find rotational speed of a 64 tooth steel wheel mounted on the main shaft.

The force measuring device is a rotating dynamometer, also referred to

as the internal balance, mounted between the rotating shroud and the main drive shaft. The internal balance consists of two parallel plates connected by four parallel bars which are strain gauged to measure the six components of force and moment. Chapter 5 discusses briefly the calibration of the internal balance. Wires from the internal balance go through a hollow shaft and flexible coupling to the slip ring assembly and then to a rack of Vishay model 2310 signal conditioning amplifiers.

Piezoelectric pressure transducers with built-in amplifiers (model 105B02) from PCB, Inc. were used for the unsteady pressure measurements. The transducer was selected because of its small size (diaphragm diameter 0.1 in.), high resonant frequency (250 kHz) and good resolution (0.01 psi). The stainless diaphragm permitted long time exposure to water. The dynamic calibration provided by the manufacturer was used. The linearity of the calibration was with 2%.

The steady pressure along the surface of the rotating shroud was measured using forty 42-inch inverted air/water manometers. A common pressure was applied to the airspace on the top of the manometers and the tubes leading from the pressure taps were connected to the bottom of each manometer. Flip valves at the base of manometer tubes allowed the pressure taps to be switched off simultaneously, thereby freezing the results once the system came to equilibrium.

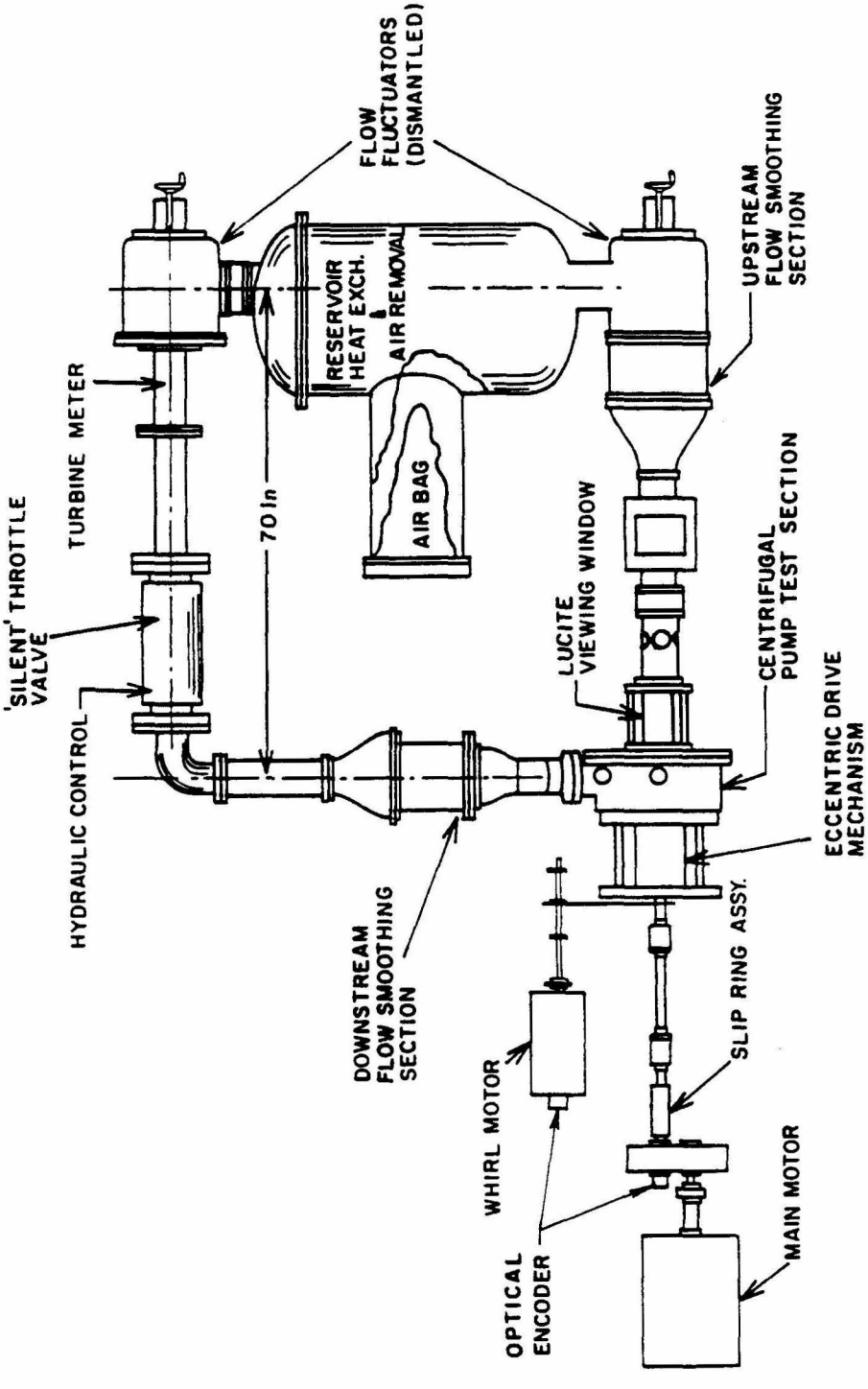

Fig. 2.1 Schematic layout of the Rotor Force Test Facility.

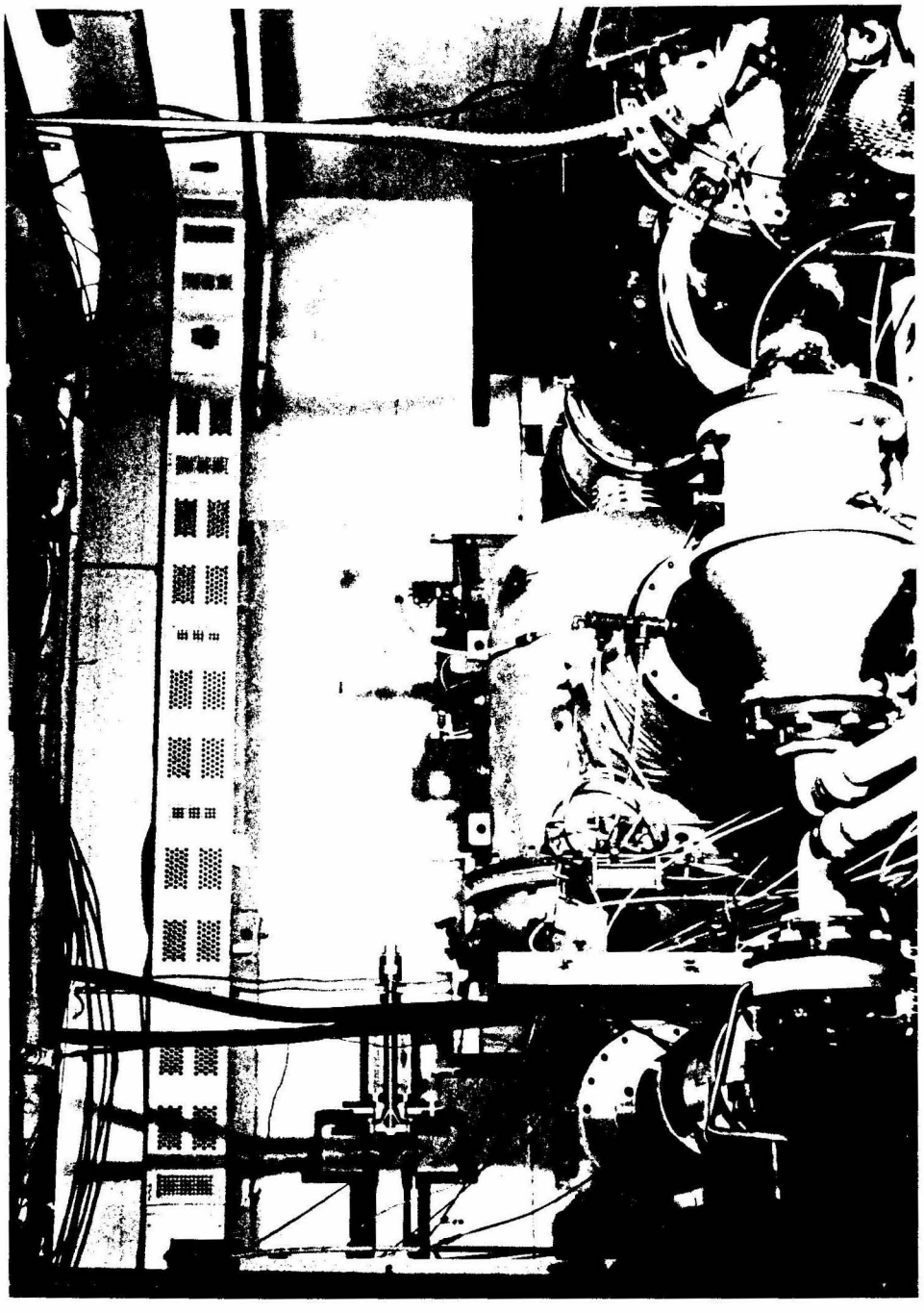

Fig. 2.2 Photograph of the Rotor Force Test Facility.

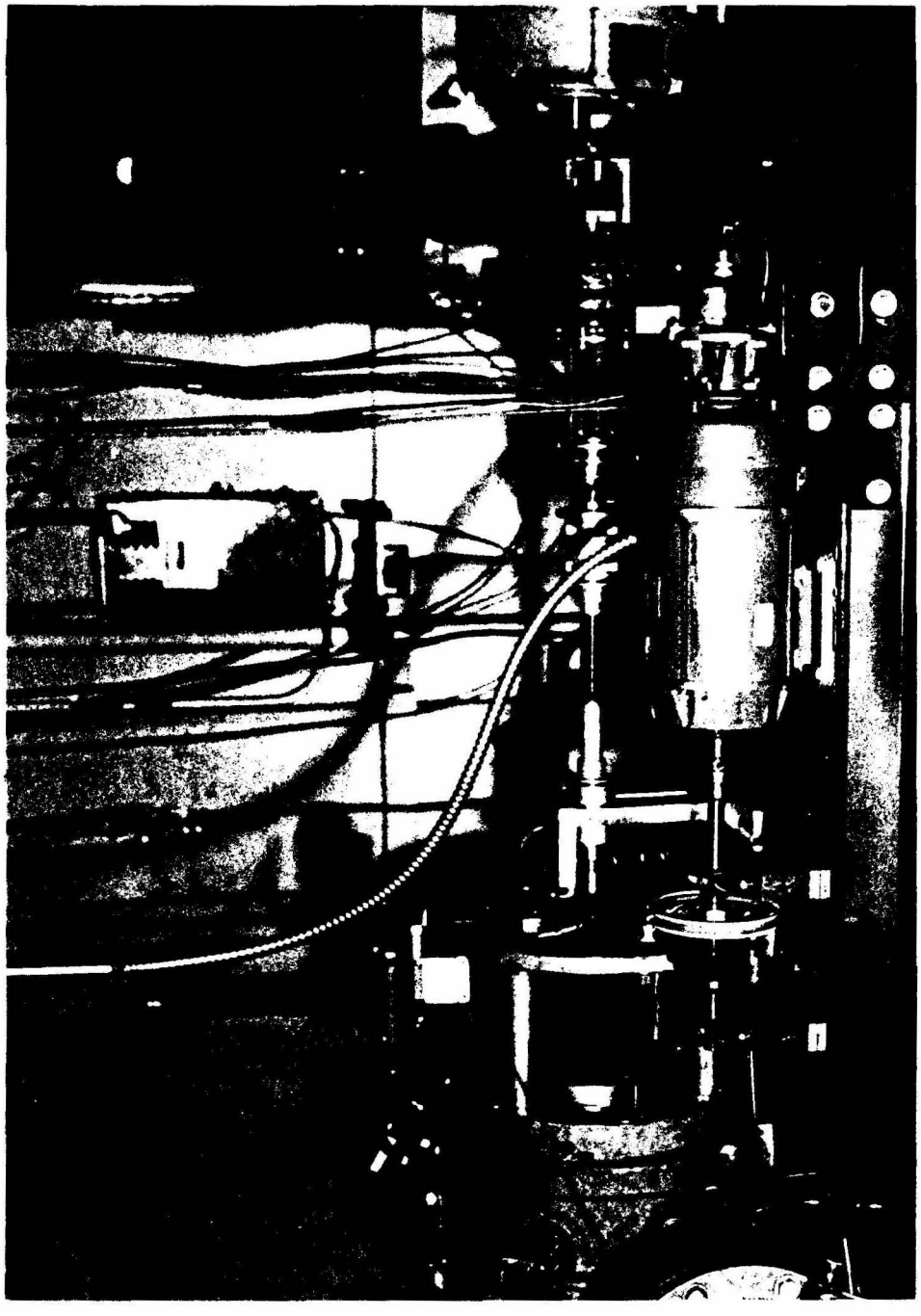

Fig. 2.3 Photograph of the drive shaft, the slip ring assembly, and the drive shaft drive box.

Chapter 3

DESIGN OF THE EXPERIMENTAL APPARATUS

The present experiment was aimed to measure forces and pressure distributions caused by the shroud leakage flow along the front shroud of an impeller. In order to eliminate other hydrodynamic forces acting on the impeller (such as impeller/volute and impeller/wear ring seal interactions) a simple rotating/stationary shroud pair was designed to meet the goals of the research. Figure 3.1 shows the assembly drawing of the designed shroud force test apparatus. The 45° cone-like geometry of the shroud surfaces was designed for easy manufacturing while without losing generality. With this apparatus setting in the loop, a front shroud leakage flow could be simulated.

Hydrodynamic forces and pressure distributions on the surface of rotating shroud are functions of the following parameters: flow coefficient ϕ, whirl ratio ω/Ω, Reynolds number R_e, and geometric parameters ε^*, H^* and δ^* (see Fig. 3.2). The head coefficient ψ could be determined by the above parameters. As far as the design of the apparatus was concerned, only setting of the geometric parameters and obtaining the force and pressure signals were needed to be considered. The rotating shroud was mounted to the spindle and the latter to the internal balance so that the shroud forces will be sensed by the internal balance. Since the width of the clearance between rotating and stationary shroud is very small, the same pressure was assumed acting on both shroud surfaces at the same radius. For convenience, pressure signals were picked up along the surface of the stationary shroud. There are three sets of steady pressure taps,

ten taps along meridional direction for each set, arranged at $\theta = 0°, 120°, 240°$, respectively. At the inlet of the leakage path, there are nine taps (including three from the three sets mentioned above) equally spaced along peripheral direction. There are two sets of dynamic pressure taps, six for each set, arranged at $\theta = 90°$ and $180°$. The seal box was designed to protect the piezoelectric pressure transducers from water.

The eccentricity ε can be adjusted by moving the stationary shroud in radial direction from 0 to 7 mm (the rotating shroud could be moved along a circular orbit with a radius of 0.01 in. in current setting of the eccentric drive mechanism). The clearance H can be adjusted by moving the stationary shroud axially from 0 to 7 mm. The seal clearance δ can be adjusted by turning the seal ring from 0 to 7 mm. The clearance H can be measured using a general depth gauge through four holes on the stationary shroud.

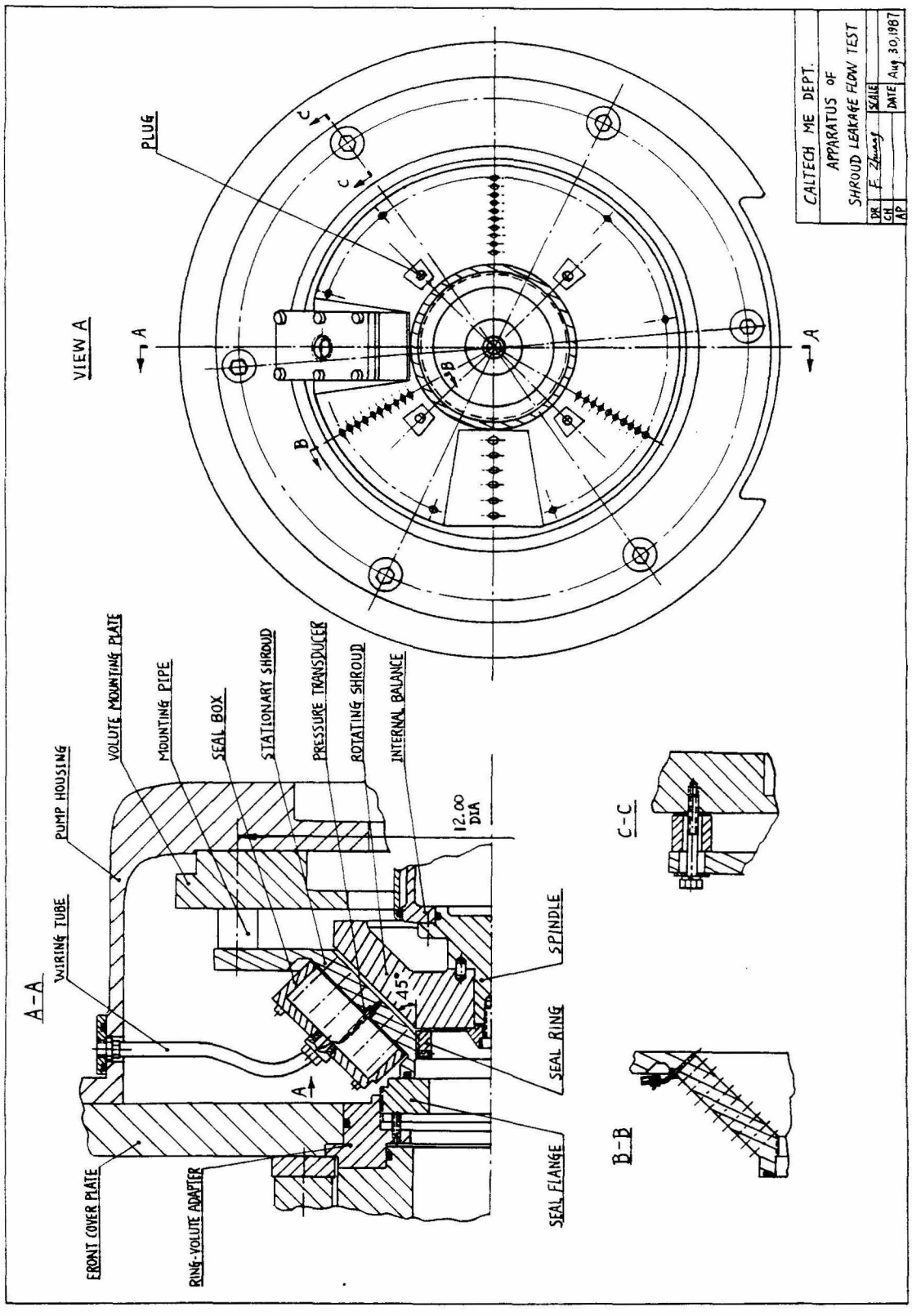

Fig. 3.1 Assembly drawing of the shroud force test apparatus.

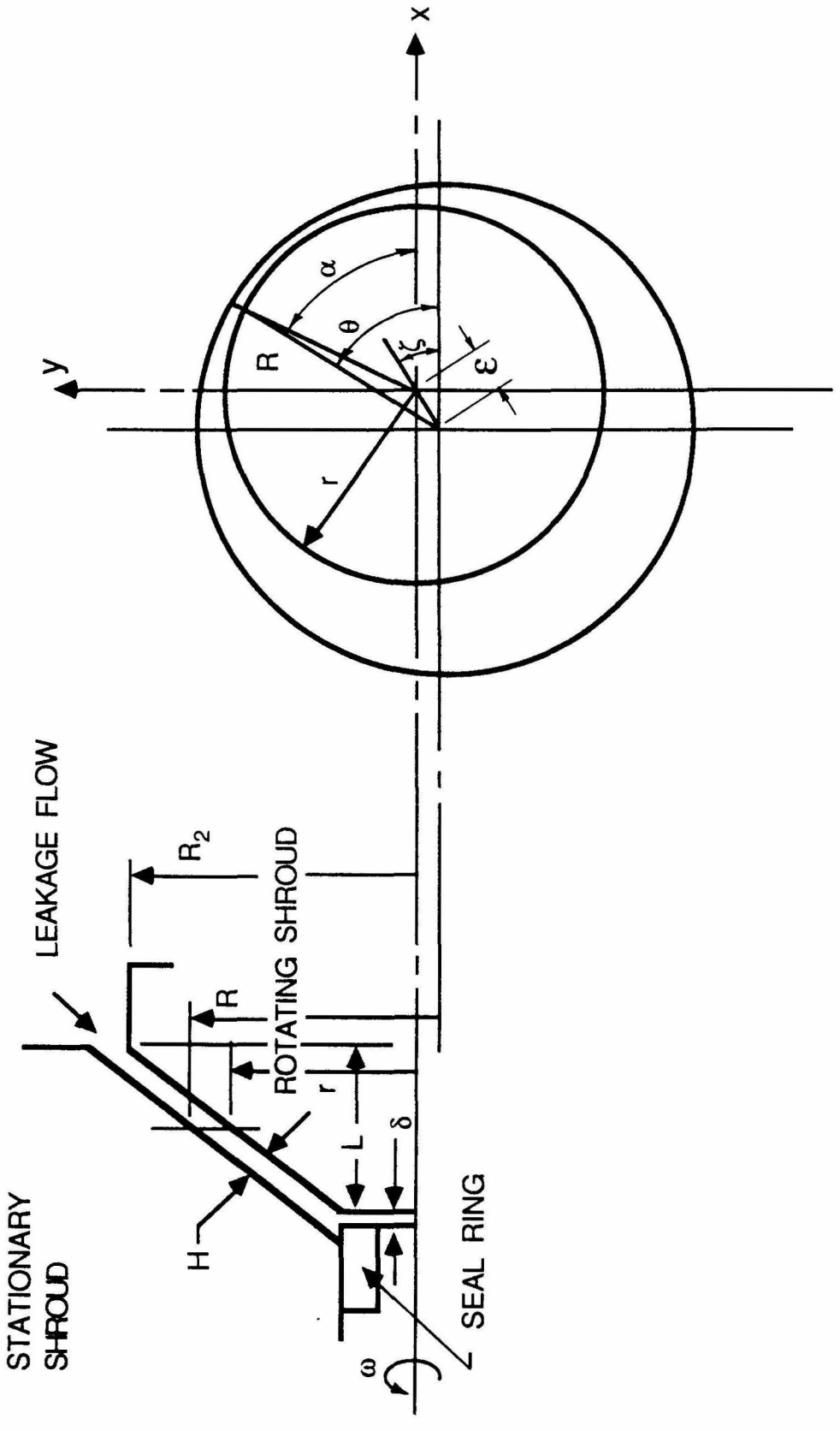

Fig. 3.2 Schematic showing geometric parameters of the shroud force test apparatus.

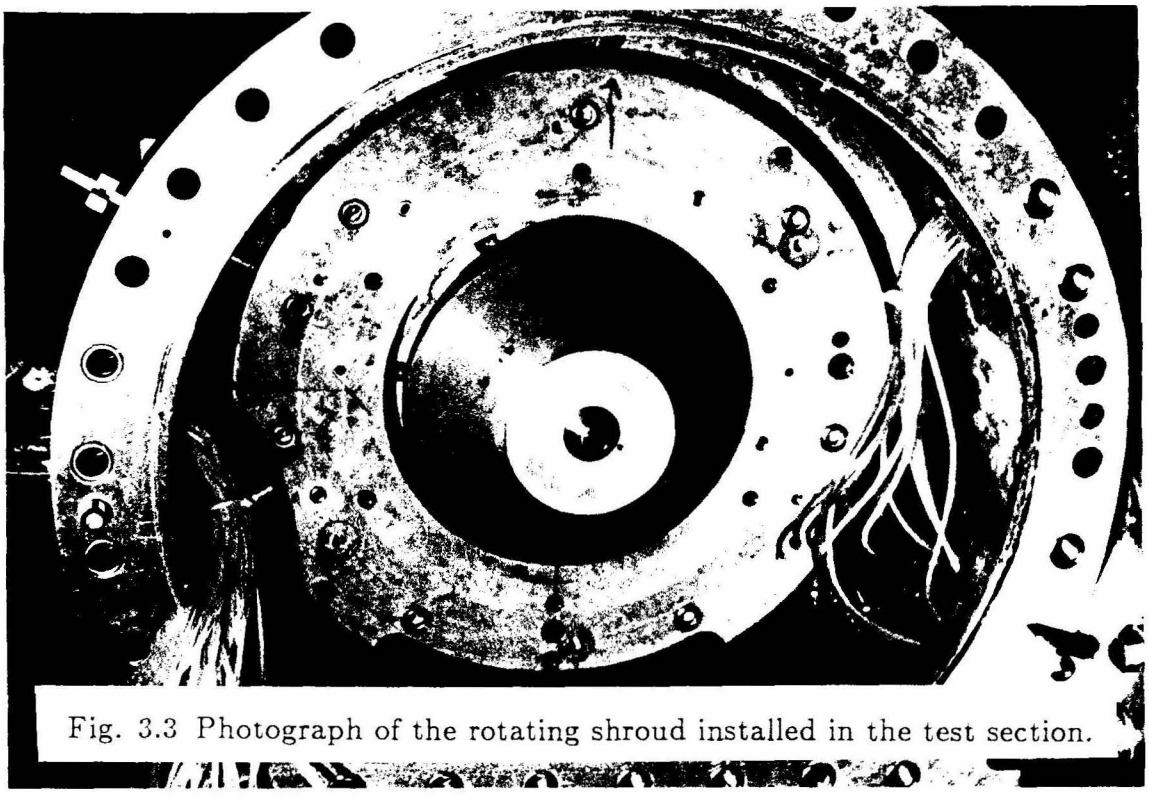

Fig. 3.3 Photograph of the rotating shroud installed in the test section.

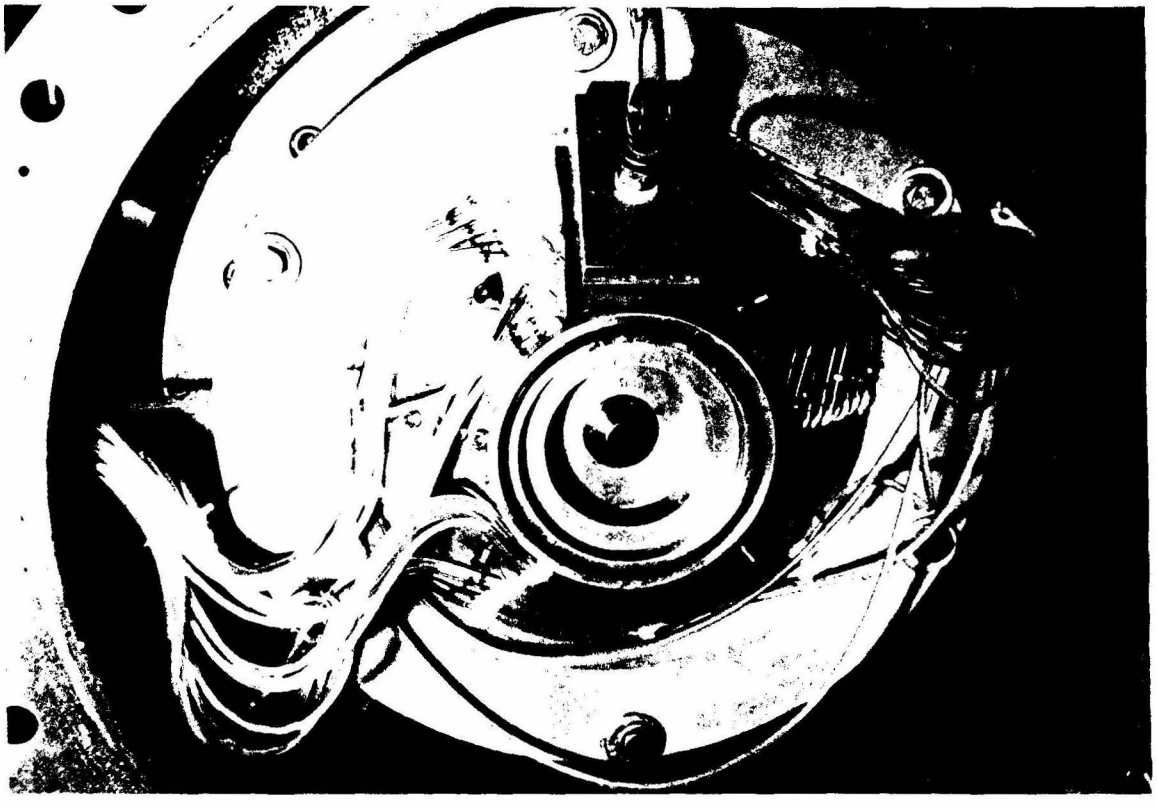

Fig. 3.4 Photograph of the stationary shroud together with seal box installed in the test section.

Chapter 4

DATA ACQUISITION AND PROCESSING

Three techniques were used in the present experimental investigation. Hydrodynamic forces were measured using the internal balance, dynamic pressure distributions were measured using a piezoelectric pressure transducer, and steady pressure distributions were measured using the air/water manometers. This chapter will explain how the data acquisitions are accomplished and data processed.

4.1. Hydrodynamic Force Measurements

The signals from the bridges of the internal balance go from the slip rings through cables across the ceiling to the rack of signal conditioning amplifiers. The amplifier outputs are sampled by a 12-bit analog-to-digital (A/D) converter and stored in the memory of a desktop personal computer. The data acquisition system has four elements, the data taker (A/D converter and computer), the closed-loop motor control systems, and a frequency multiplier/divider which synchronizes the previous three elements. Given an input TTL signal by a Wavetek model 171 synthesizer/function generator and two thumb wheel selected integers, I and J, the frequency multiplier/divider outputs the following pulse signals: N (clock frequency for main motor command, $1024 * \omega$), NI/J (clock frequency for whirl motor command, $1024 * \Omega$), N/J (clock frequency for starting the A/D conversion, $1024 * \omega/J$), and N/J (index frequency for synchronizing reset, ω/J). In this experiment, whirl motor was not used. The clock

frequency is equal to 1024*index frequency because the feedback for the motor control is provided by an optical encoder which outputs two signals: an index pulse at every revolution and a clock of 1024 pulses per revolution. The N/J index output starts the data taking process and synchronizes phase control of the motors. The data taker can sample up to sixteen channels. The first channel is sampled at N/J index pulse (time = 0). Subsequent samples are taken by following the N/J clock signal. The 1024 samples per data taking cycle are divided among six bridges of the internal balance at 128 points/bridge/cycle leaving four channels at 64 points/channel/cycle. The four remaining channels were connected to the upstream and downstream pressure transducers, the flow meter and the shaft torque bridge (the results from them were not used for this investigation). 256 cycles of data were taken to average, the instantaneous data (8*64k bytes) were occasionally stored for subsequent processing.

In this experiment, no whirl motion was performed. Equation (1.2) can be expressed as

$$\begin{Bmatrix} F_x \\ F_y \end{Bmatrix} = \begin{Bmatrix} F_{ox} \\ F_{oy} \end{Bmatrix} + \varepsilon \begin{bmatrix} A_{xx} & A_{xy} \\ A_{yx} & A_{yy} \end{bmatrix} \begin{Bmatrix} \cos\varsigma \\ \sin\varsigma \end{Bmatrix} \tag{4.1}$$

where ς is the angular location of the rotating shroud center (see Fig. 4.1). The rotating shroud was positioned at four eccentric positions (ς = 0, 90, 180, 270 degrees) relative to the stationary shroud. Once the x and y force components are obtained from each of the four positions, the elements of the force matrix (they are equal to the elements of the stiffness matrix in this situation) are calculated by

$$
\begin{aligned}
A_{xx} &= \left(F_x(0) - F_x(180)\right)/2\varepsilon \\
A_{xy} &= \left(F_x(90) - F_x(270)\right)/2\varepsilon \\
A_{yx} &= \left(F_y(0) - F_y(180)\right)/2\varepsilon \\
A_{yy} &= \left(F_y(90) - F_y(270)\right)/2\varepsilon
\end{aligned}
\tag{4.2}
$$

and the averaged forces are

$$
\begin{aligned}
F_{ox} &= \left(F_x(0) + F_x(90) + F_x(180) + F_x(270)\right)/4 \\
F_{oy} &= \left(F_y(0) + F_y(90) + F_y(180) + F_y(270)\right)/4
\end{aligned}
\tag{4.3}
$$

Referring to Fig. 4.1 the lateral forces in the laboratory frame, F_x and F_y, are related to the lateral forces detected by the internal balance in the rotating frame, F_1 and F_2, by a rotation through the angle $-(\omega t + \frac{\pi}{2})$, where ω is the frequency of main shaft rotation,

$$
\begin{aligned}
F_x(t) &= -F_1(t)\sin\omega t - F_2(t)\cos\omega t \\
F_y(t) &= F_1(t)\cos\omega t - F_2(t)\sin\omega t
\end{aligned}
\tag{4.4}
$$

$F_1(t)$ and $F_2(t)$ are extracted from the raw data in terms of their Fourier coefficients (the subscript denotes the cos or sin, respectively, Fourier coefficient. The superscript refers to the order of the coefficients).

$$
\begin{aligned}
F_1(t) &= F_1^0 + \sum_{i=1}^{\infty} F_{1_s}^i \sin\left(i\omega t/J\right) + F_{1c}^i \cos\left(i\omega t/J\right) \\
F_2(t) &= F_2^0 + \sum_{i=1}^{\infty} F_{2_s}^i \sin\left(i\omega t/J\right) + F_{2c}^i \cos\left(i\omega t/J\right)
\end{aligned}
\tag{4.5}
$$

Substitute (4.5) into (4.4) and perform the following integrations to get time averaged lateral force F_x and F_y:

$$F_x = \frac{1}{T}\int_0^T F_x(t)dt = -\frac{1}{2}\left(F_{1s}^J + F_{2c}^J\right)$$
$$F_y = \frac{1}{T}\int_0^T F_y(t)dt = \frac{1}{2}\left(F_{1c}^J - F_{2s}^J\right) \tag{4.6}$$

Where $T = NCYC * J/\omega$, and $NCYC$ is the number of cycles of reference frequency used for taking data. In the present experiment, $NCYC = 256$.

The radial force, $[A]\varepsilon$, due to the eccentricity of the rotating shroud, can also be resolved into its components, F_n and F_t, normal to and tangential to the whirl orbit. The normal force is considered positive radially outward. The tangential force is considered positive when in the direction of the velocity of the whirl motion. If the elements of the force matrix have the property $A_{xx} = A_{yy}$ and $A_{xy} = -A_{yx}$, then F_n and F_t for the whirl orbit can be expressed as

$$F_n = \frac{1}{2}\left(A_{xx} + A_{yy}\right)\varepsilon$$
$$F_t = \frac{1}{2}\left(-A_{xy} + A_{yx}\right)\varepsilon \tag{4.7}$$

To obtain experimentally the fluid-induced forces acting on the surface of the rotating shroud, two identical tests are performed, one in air (without stationary shroud installed) and the other in water, in other words, a "dry" run and a "wet" run. The forces from the former experiment are subtracted from the latter to yield the fluid-induced forces. The buoyancy force on the rotating

shroud, obtained from half the difference in tests taken in water and in air with the impeller rotated through 180 degrees, is also subtracted.

4.2. Unsteady Pressure Measurements

The signals from the piezoelectric transducers are sampled in a 16 channel data acquisition system and stored in the memory of a desk top computer (used also for force measurements). The closed-loop motor control system is used in this experiment. The data taken is triggered by N/J index signal from the frequency multiplier/divider directly instead of by an index signal from the shaft encoder, as in Arndt's experiment. Using one channel of the A/D converter only, data was taken at every N/J clock pulse. For a shaft speed up to 1600 rpm, 1024 data per revolution of rotating shroud were taken; for shaft speeds exceeding 1600 rpm, 512 data were taken. Both instantaneous and ensemble averaged data were stored.

The unsteady measurements are presented as an unsteady pressure coefficient, normalized by the dynamic pressure based on rotating shroud tip speed,

$$\tilde{c}_p = \frac{\tilde{p}}{(1/2)\rho u_2^2} \tag{4.8}$$

The unsteady measurements were ensemble averaged to reduce noise. The ensemble averaged unsteady pressure measurements are presented as an ensemble averaged pressure coefficient, and were obtained from the unsteady pressure coefficient by

$$\tilde{c}_{p,av}(j) = \sum_{i=1}^{N} \frac{\tilde{c}_p(i,j)}{N} \tag{4.9}$$

where i denotes the i^{th} sampling period, j denotes the j^{th} data point of the sampling period, and N denotes the total number of sampling periods. So in the process of ensemble averaging, an average is obtained for measurements made at identical orientations of the rotating shroud. The number of sampling periods used in this experiment is 512.

4.3. Steady Pressure Measurements

The steady pressure readings are taken from 38 manometers; 36 of them are connected to the pressure taps on the surface of the stationary shroud. The other two are used to read downstream pressure and the pressure on the wall of the pump housing, respectively.

As mentioned in Chapter 3, the pressure on the surface of the rotating shroud is assumed to be the same as on the surface of the stationary shroud at a corresponding point because of the small clearance between them. The pressures in the annular gap were integrated to obtain the net force acting on the rotating shroud. The pressure on the surface of the rotating shroud changes along both axial and circumferential directions. Since there are ten pressure taps along the meridional direction for each of the three sets of pressure taps, the rotating shroud is divided into ten regions axially, in correspondence with the pressure taps. For each region, the steady pressure distribution along the circumferential direction was obtained by fitting a third order periodic spline

through the measured data. A periodic spline fit was chosen to get continuity for the pressure and the first two pressure derivatives along the circumferential direction. Hence, the radial pressure forces are given as

$$F_x(\varsigma) = \frac{\sqrt{2}}{2} \sum_{i=1}^{10} \int \int_{s_i} p_i(\theta, \varsigma) \cos \alpha_i ds_i$$

$$F_y(\varsigma) = \frac{\sqrt{2}}{2} \sum_{i=1}^{10} \int \int_{s_i} p_i(\theta, \varsigma) \sin \alpha_i ds_i \tag{4.10}$$

where i denotes the number of the axially divided regions mentioned above, s is the surface area of the region, p the steady pressure applied on the region, and α represents the angular position on the rotating shroud surface. Because of the eccentricity, α is usually different from θ, the angular position on the surface of the stationary shroud, for a certain point on the surface of stationary shroud where pressure signal was taken. α could be expressed as (refer to Fig. 3.2)

$$\alpha_i = \tan^{-1} \left(\frac{\sin \theta - \frac{\varepsilon}{R_i} \sin \varsigma}{\cos \theta - \frac{\varepsilon}{R_i} \cos \varsigma} \right) \tag{4.11}$$

Using equations (4.1), (4.2), (4.3), (4.7), the forces can then be used to estimate the average force on the centered rotating shroud and the stiffness forces caused by the rotating shroud displacement.

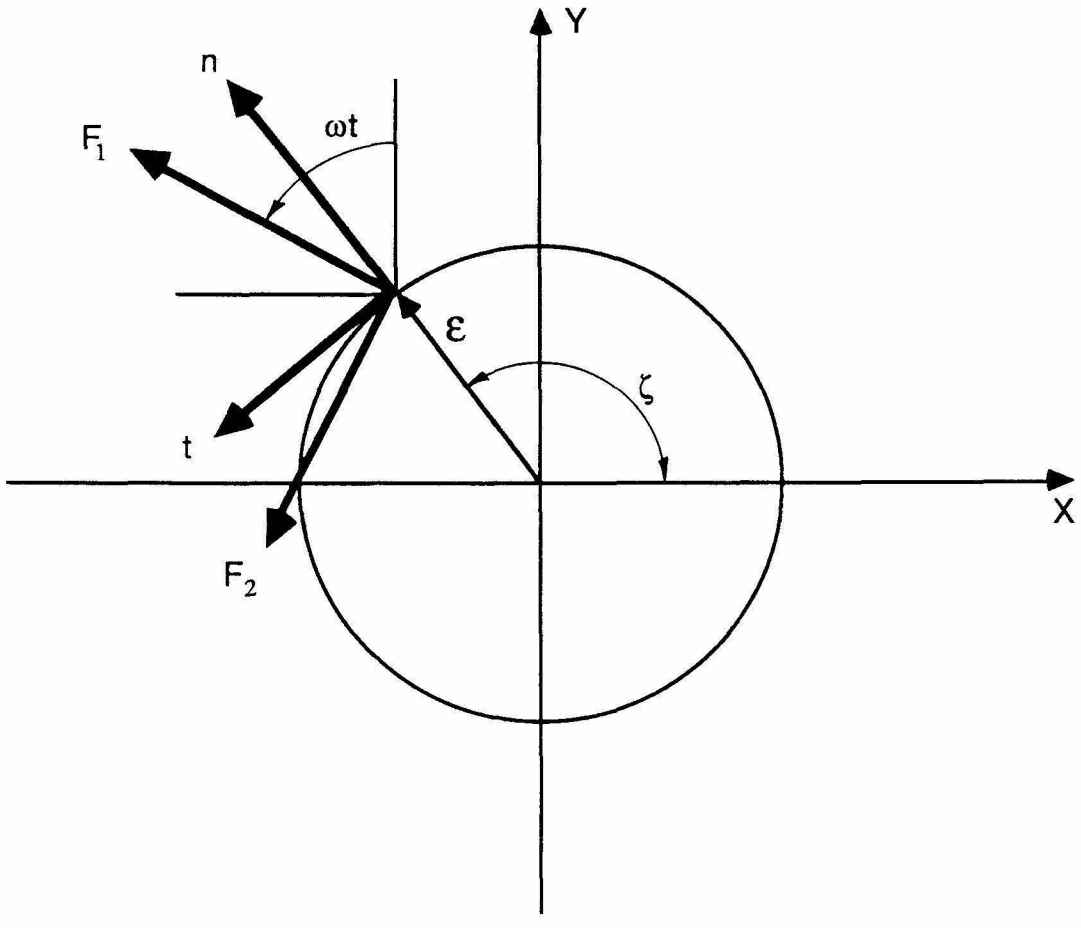

Fig. 4.1 Schematic representation of the lateral forces in the rotating dynamometer frame, F_1 and F_2, on the rotating shroud eccentrically located within the stationary shroud. X and Y represent the stationary laboratory frame; n and t represent the polar coordinate frame, normal and tangential to the whirl orbit.

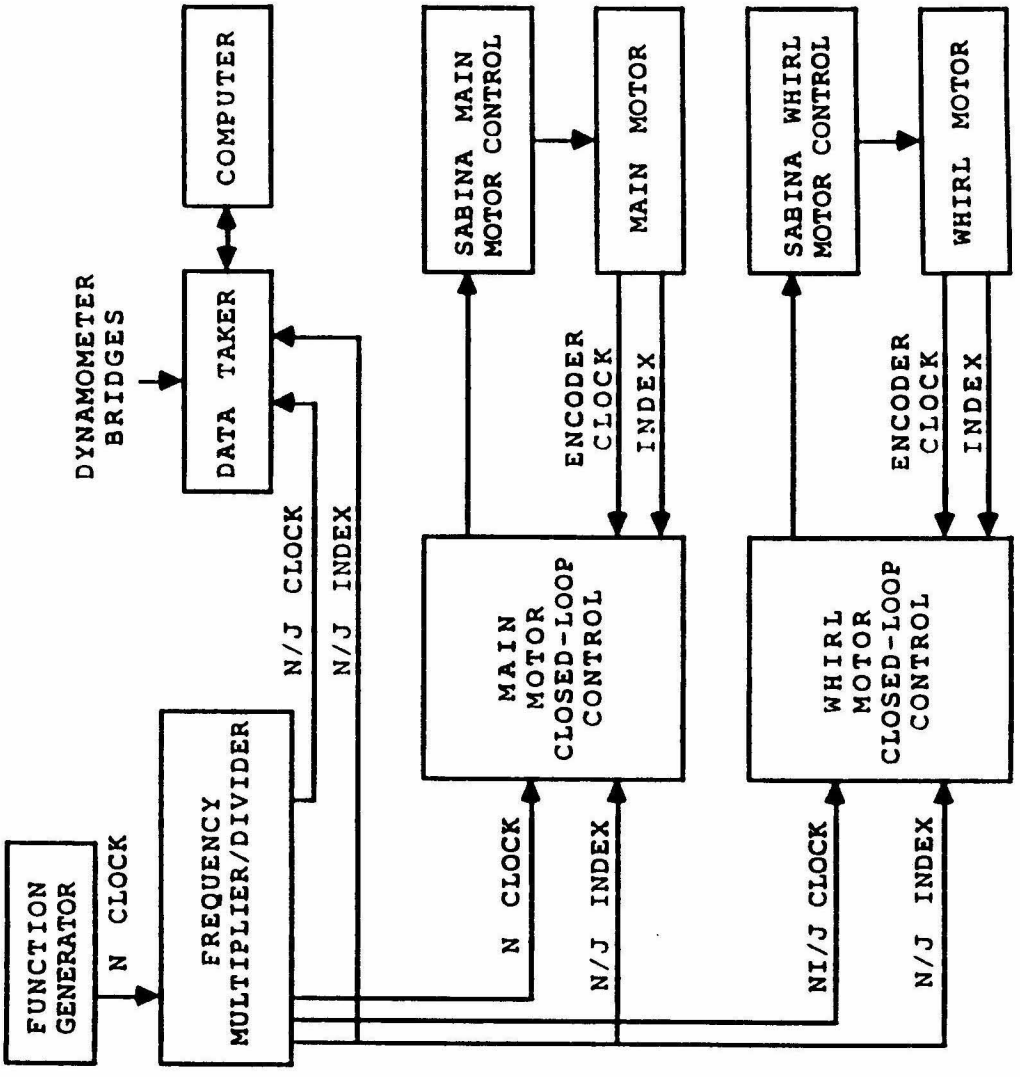

Fig. 4.2 Block diagram of the data acquisition system showing the motor control system and the data taker.

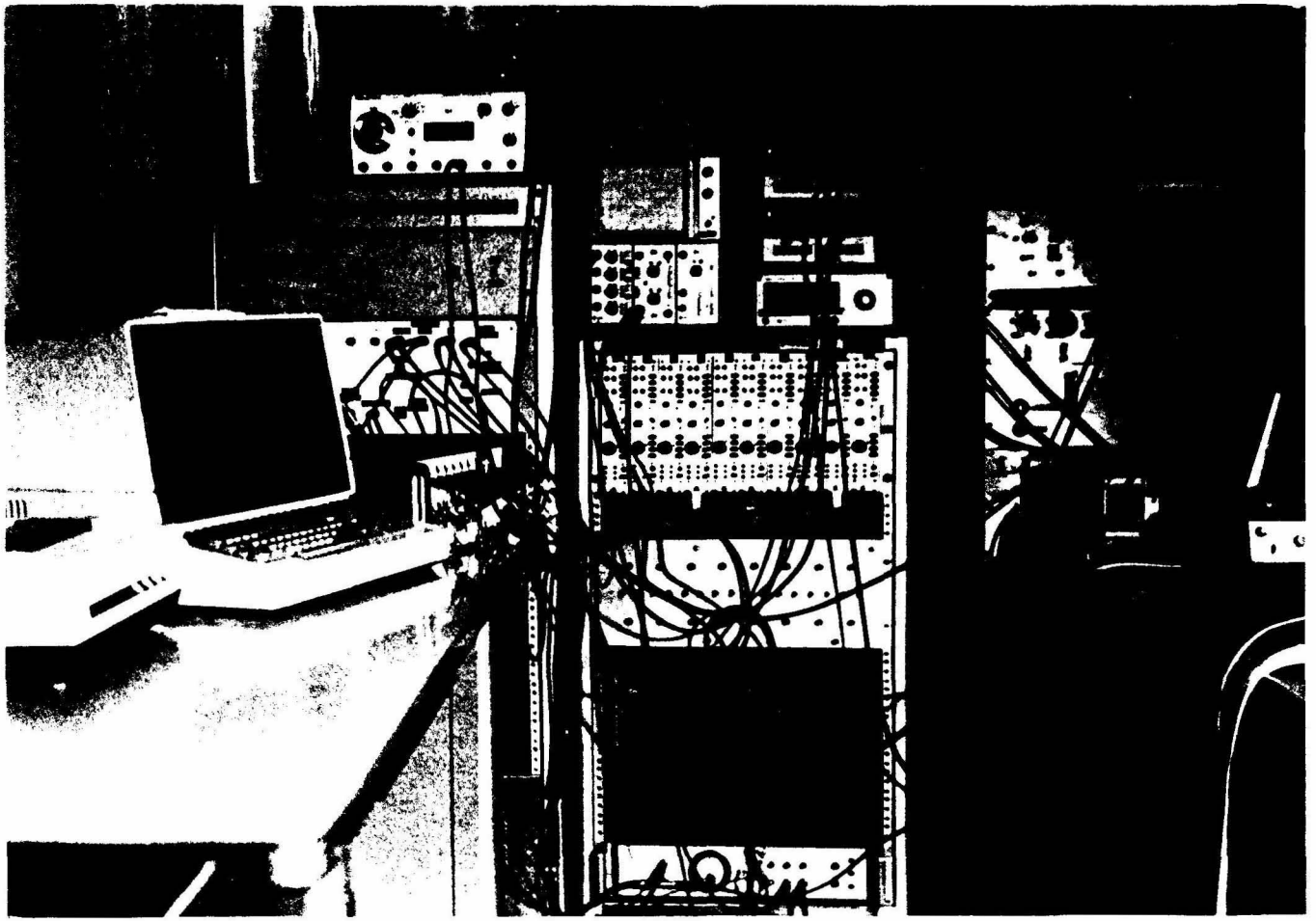

Fig. 4.3 Photograph of instrumentation. Visible are, in particular, the Zenith Z-120 computer (far left), the A/D converter (to the right of the computer), the frequency multiplier/divider (middle of the left rack), a battery of 10 signal conditioning amplifiers (top of the middle rack), closed-loop control box for main motor (bottom of the middle rack).

Chapter 5

CALIBRATION OF ROTATING DYNAMOMETER

The dynamometer, also referred to as the internal balance, is mounted between the rotating shroud and the main drive shaft. It consists of two parallel plates connected by four parallel bars of square cross section, forming a monolithic stainless steel structure. The bars are instrumented to measure the six components of force and moment with thirty-six strain gauges, forming nine Wheatstone bridges. One bridge is primarily sensitive to thrust, each of the other eight is sensitive to two of the remaining five generalized force components. Six out of nine bridges are chosen to use in the experiment.

5.1 Static Calibration

Calibration of the internal balance consisted of static force loadings and dynamic tests. The purpose of the static calibration is to produce a six-by-six calibration matrix, $[B]$, which would include all possible internal balance interactions. The six-component force vector, $\{F\}$, can then be obtained from the measured bridge out voltages by use of the relation $\{F\} = [B]\{V\}$. Where $\{V\}$ is a six-component voltage vector.

The matrix $[B]$ is simply the inverse of the matrix of slopes, $[S]$, in which an element, S_{ij}, represents the output voltage, V_i of bridge i under a unit load of j^{th} force component F_j. The slopes, S_{ij}, are determined by six sets of individual force loadings, one for each generalized force component.

In the present experiment, since the main concern is about the lateral forces

acting on the rotating shroud, it was decided to check the slopes for the lateral forces, namely, F_1 and F_2. A rig of pulleys, cables and weights was used to apply loadings on the internal balance in both positive and negative directions of F_1 and F_2. Each set comprised nine such loadings, ranged from 0 to 30 lbs.

The results show that under the loadings in F_1 and F_2 directions the response of the bridges are linear and the slopes are very close (within 1.5%) to the next previous calibration (Franz [1987]). Fig. 5.1 shows a typical calibration graph. At this point, it was decided to use the same calibration matrix (version k, Franz [1987]) for the present experiment.

5.2. Dynamic Behavior

The rotating shroud was mounted to a spindle, which is connected to the internal balance. By rotating the main shaft in the air, the internal balance will sense the weight of the rotating shroud and the spindle. In the rotating frame, the force on the internal balance is

$$\begin{aligned} F_1(t) &= -mg\cos(\omega t) \\ F_2(t) &= mg\sin(\omega t) \end{aligned} \tag{5.1}$$

where m is the mass of the rotating shroud and the spindle and g is the gravitational constant. The steady term which depends on the orientation of the internal balance when the bridge amplifier outputs were zeroed is not shown. The magnitude and phase error of this radial force is presented in Figure 5.2. For the components, F_1 and F_2, the magnitude is within 3% and the phase error is less than 2 degrees.

In addition to the rotating test, a lateral impulse load was applied to the rotating shroud, which was stationary, in both F_1 and F_2 directions. The responses from the six selected bridges and two accelerometers placed on the back plate of the eccentric drive were collected. This test is also referred to as the hammer test. Figure 5.3 shows the spectrum of the data from bridge 8, which is sensitive to the lateral force F_1, under a lateral impulse load in F_1 direction. The peak at 200 Hz corresponds to the damped lateral vibration natural frequency of the internal balance with the rotating shroud mounted. This frequency is much higher than the shaft rotating frequencies planned for this experiment.

Since the internal balance performed well under dynamic tests, the static calibration matrix was deemed to be sufficient to process the dynamic measurements.

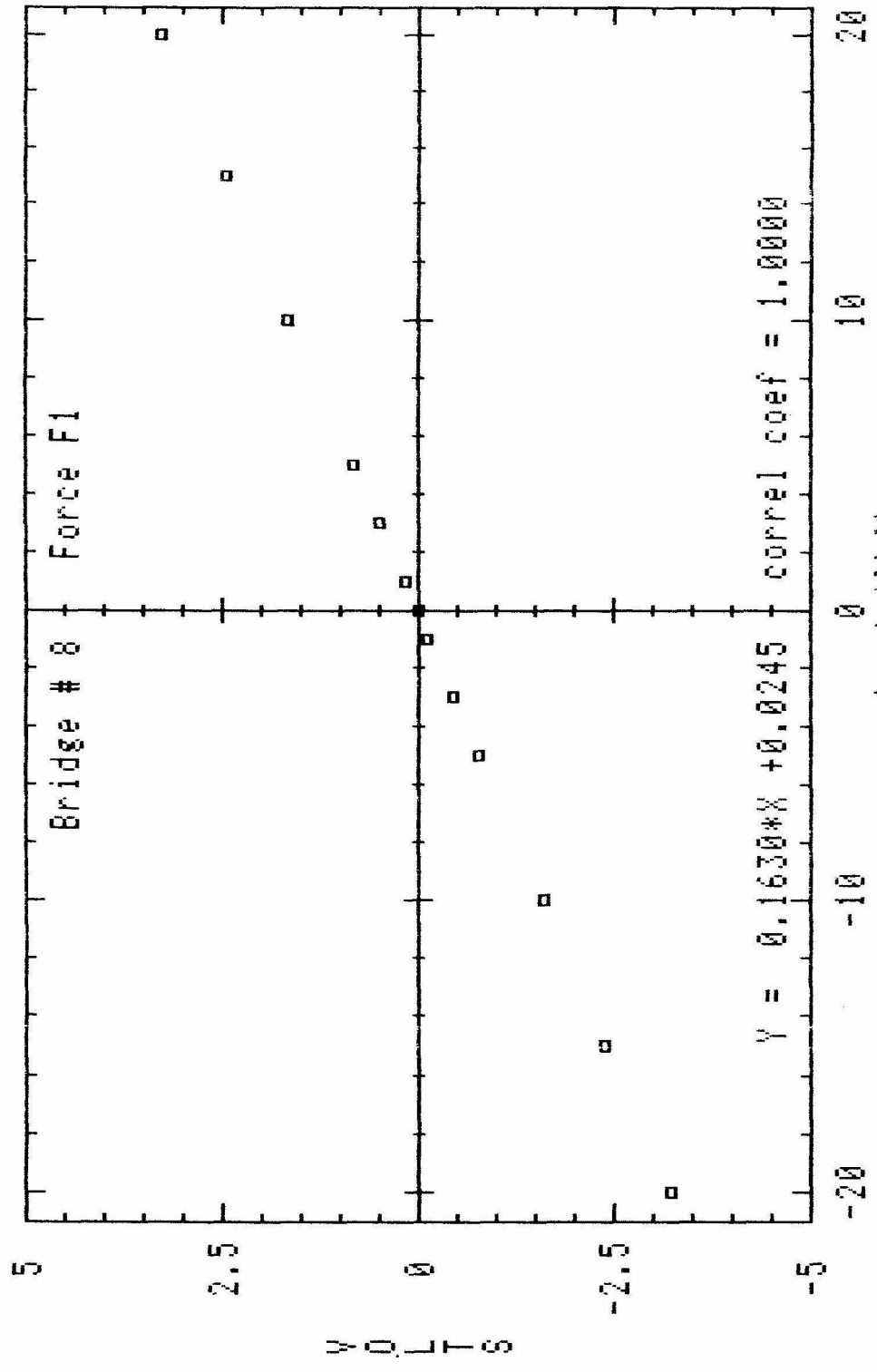

Fig. 5.1 A typical in-situ static calibration loading graph. Bridge 8 is primarily sensitive to loading in F_1 direction.

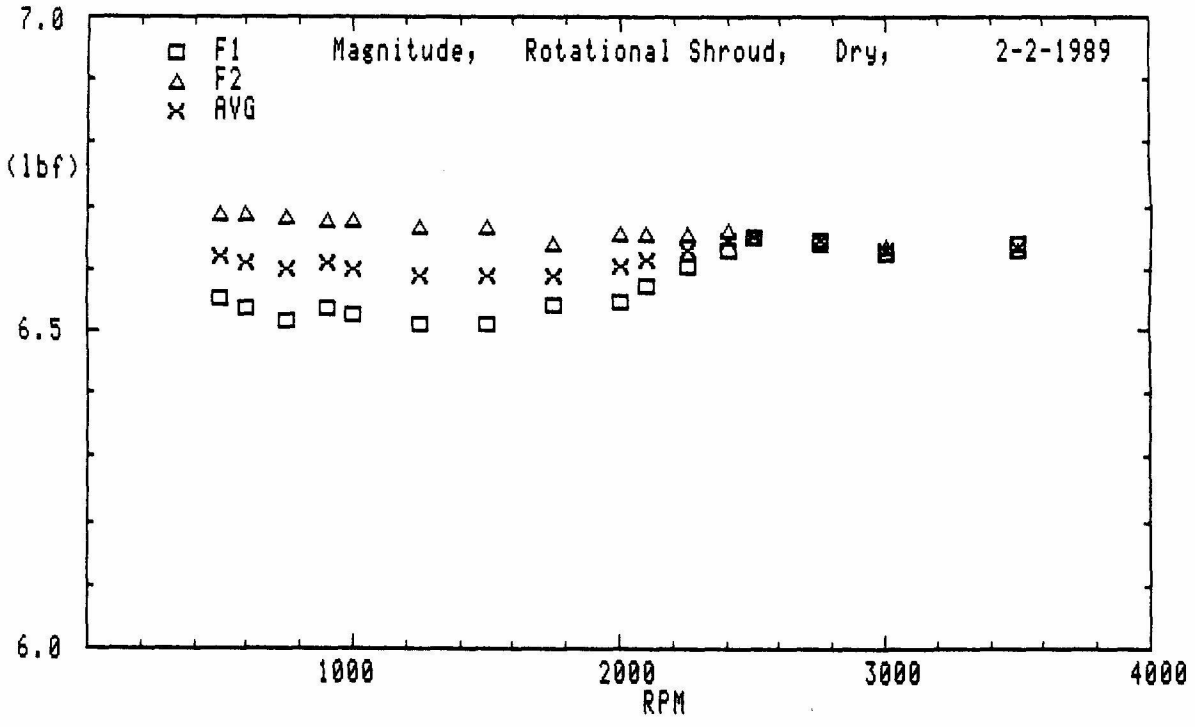

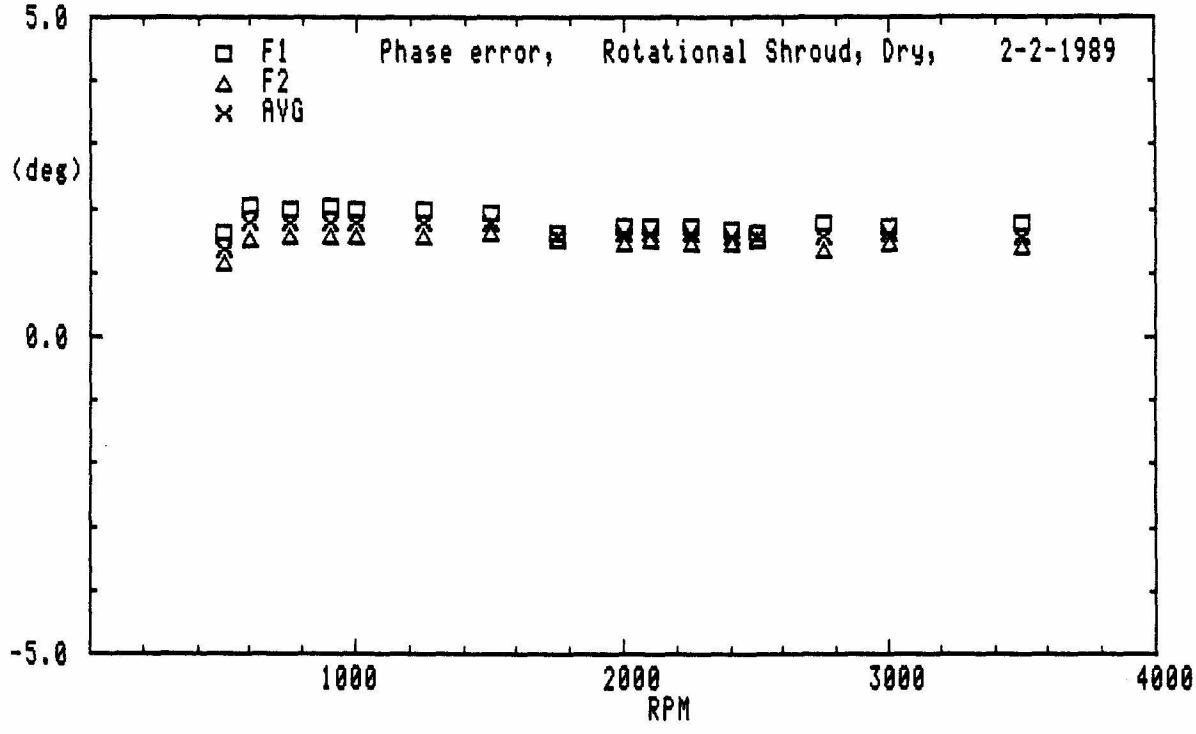

Fig. 5.2 The weight of rotating shroud is sensed as a rotating force vector in the frame of the dynamometer (F_1, F_2). Plotted are (a) the magnitude and (b) the phase error from rotating the shaft in air at various speeds.

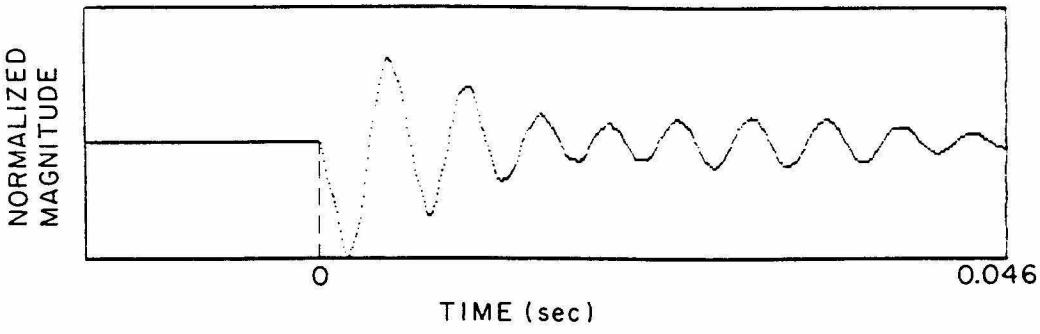

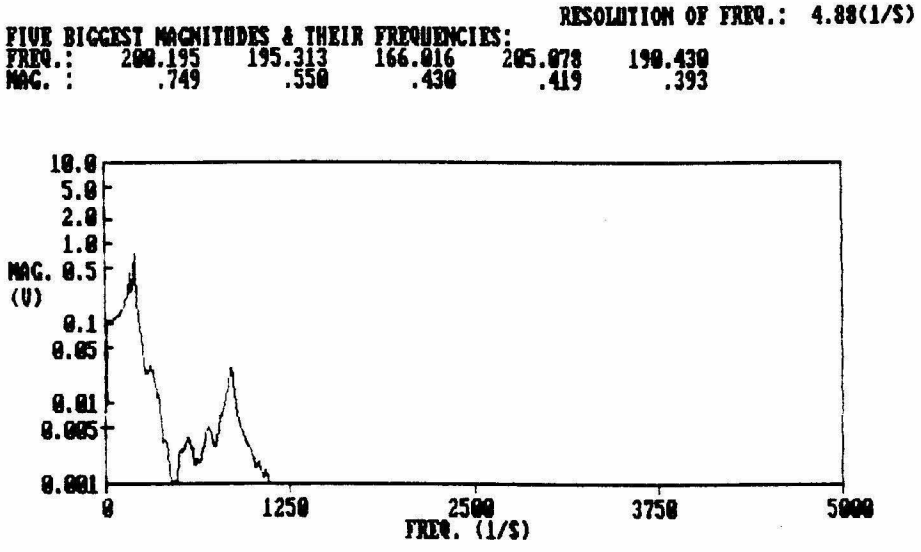

Fig. 5.3 Magnitude spectrum of bridge 8 showing the response of the dynamometer-shaft system to a lateral impulse (hammer test) applied to rotating shroud in F_1 direction. The damped natural frequency is at 200 Hz.

Chapter 6

EXPERIMENTAL PROCEDURE

6.1. Set Up of the Experimental Apparatus

It is important for a good measurement to get relatively accurate geometry for both rotating and stationary shrouds and place them in the proper position. When the rotating shroud was first mounted, the maximum position error in radial direction along the shroud surface was .003 in. After rebuilding the journal of the spindle, the error was reduced to .0013 in., which might be the best that can be obtained because the internal balance itself has .001 in error in radial direction. The position error in axial direction is .0002 in for the rotating shroud. In order to make the stationary shroud axis parallel to the axis of the rotating shroud, the position of the volute mounting plate was adjusted by putting shims between the volute mounting plate and pump housing and using mounting pipe with accurate length ($\pm$.0002 in.) between the stationary shroud and volute mounting plate. Compared with the width of the clearance chosen in the experiment (ranged from .055 to .167 in.), the position error in radial direction (.0013 in.) is very small.

In this experiment, the rotating shroud was set in one position, usually the top position of the eccentric drive. The eccentricity ε was obtained by setting the stationary shroud center to four different positions ($\varsigma = 0, 90, 180, 270$ degrees) around rotating shroud center with distance ε. Width of clearance H was set by using different mounting pipes. For a certain clearance H and eccentricity ε, considering the positions of the holes through which H can be measured, the

relation between δ_H (the change of H) and ε can be calculated by

$$\delta_H = \pm \left\{ \frac{\varepsilon^2}{4(R_o\sqrt{2} - H) + 2\varepsilon} + \frac{\varepsilon}{2} \right\} \tag{6.1}$$

where S is the inner radius of the stationary shroud at the point of measurement. There are four points (equally spaced holes) on the stationary shroud for clearance measurement. Using a depth gauge, $(H + \delta_H)$ will be read from two holes and $(H - \delta_H)$ the other two, provided that the thickness of the stationary shroud is subtracted. Setting a planned eccentricity was sometimes difficult. The error between the planned eccentricity and the one actually obtained was within 3%.

6.2. Test Variables

Measurements for three different eccentricities ε, three different clearances H, two face seal clearances δ, and five shaft rotative speeds were planned. Dry runs were first performed with the rotating shroud rotating in air. The stationary shroud was removed. A water jet was used to lubricate the eccentric drive inner face seal. Besides measuring the force experienced by the internal balance due to the mass of the rotating shroud, the dry runs check the dynamic behavior of the internal balance and verify the orientation of the optical encoder on the main drive shaft.

A group of measurements for $\varepsilon = 0.038$, $H = 0.084$, RPM=1500 and $\delta = 0.185$ were then performed for $\varsigma = 0°, 90°, 180°$ and $270°$. It was found that the force matrix were approximately skew-symmetric. A test matrix was then

made (see table 6.1). Using the property of skew-symmetric force matrix, only one combination of ε, H, δ was tested for $\varsigma = 0°, 90°, 180°$ and $270°$, the rest of the tests were scheduled only for $\varsigma = 0°$ and $180°$.

The range of the shaft rotating speeds (500 to 1750) was chosen for the pressure data to lie within the manometer range. The flow rate in this experiment was generated by the rotating of the rotating shroud and restricted by the face seal clearance. It was very small (a few GPM) and not measured in this experiment.

Since no whirl motions of the rotating shroud were performed, the flow was expected to be steady, only one piezoelectric pressure transducer was installed on the top second tap of the vertical group of taps on the stationary shroud.

After each measurement, the data were processed to yield radial force acting on the rotating shroud. For the measurements from the internal balance, the corresponding dry runs were subtracted to eliminate the force of gravity and possible centrifugal force on the rotating shroud. The buoyancy force was also subtracted, leaving only the hydrodynamic force on the rotating shroud. The pressure along the surface of the rotating shroud was integrated to get radial force. The radial forces are presented in the next chapter in terms of F_o and hydrodynamic force matrix $[A]$ due to the eccentric location of the rotating shroud. In this experiment, $[A]$ could be considered hydrodynamic stiffness matrix because whirl speed is zero. The force due to the eccentric location of the shroud will also be presented by the average force normal to and tangential to the whirl orbit, F_n and F_t.

	$\zeta = 0^\circ, 180^\circ$ $\varepsilon = 0.038$ in	$\zeta = 0^\circ, 180^\circ$ $\varepsilon = 0.076$ in	$\zeta = 0^\circ, 90^\circ$ $180^\circ, 270^\circ$ $\varepsilon = 0.150$ in
H = 0.055 in	1000 rpm 1500 rpm	—	—
H = 0.084 in	1000 rpm 1500 rpm	—	—
H = 0.167 in	1000 rpm 1500 rpm	1000 rpm 1500 rpm	750 rpm 1000 rpm 1250 rpm 1500 rpm 1750 rpm

Table 6.1. Tests performed after the preliminary tests (the front face seal clearance for the tests listed above is 0.020 in).

Chapter 7

PRESENTATION OF DATA AND DISCUSSION

The hydrodynamic forces and steady and unsteady pressure distributions on the surface of the rotating shroud were measured as functions of eccentricity, shroud clearance, face seal clearance and shaft rotating speed. Emphasis is placed on the hydrodynamic force matrices $[A]$, which contain the essence of the information sought. Some of the measurement results are compared with limited experimental and theoretical data available from other sources. Measurements from the internal balance and manometers compared fairly well.

7.1. Hydrodynamic Force Matrix [A]

For all four positions $\varsigma = 0°, 90°, 180°$ and $270°$, experiments were conducted for two geometry combinations, one for $\varepsilon = 0.038$ in, $H = 0.084$ in, $\delta = 0.185$ in, and the other one $\varepsilon = 0.150$ in, $H = 0.167$ in, $\delta = 0.020$ in, the latter was conducted under six different shaft speeds. Elements of the force matrix are extracted using the formulas in Chapter 4. The diagonal elements, A_{xx} and A_{yy}, are grouped in Fig. 7.1, and the off-diagonal elements, A_{xy} and A_{yx}, in Fig. 7.2. Both are plotted against the shaft speeds.

Examination of the results from the above two tests shows that matrix $[A]$ has almost equal diagonal terms, and off-diagonal terms which are almost equal but opposite in sign. It indicates that, same as the matrix $[A]$ for total hydrodynamic force acting on the impeller (Chamieh (1983) and Jery (1987)), the matrix $[A]$ for the hydrodynamic shroud force itself is also skew-symmetric.

This result qualitatively agrees with Adkins (1986) pressure measurements along a rather big shroud annular gap.

The values of F_n and F_t corresponding to the data in Figure 7.1 and 7.2 are presented in Figure 7.3. Considering first F_n, note that the hydrodynamic force is always in the radially outward direction. The sign of the tangential force, F_t, is encouraging forward whirl motion of the rotating shroud.

7.2. Effect of Reynolds Number

In this experiment the Reynolds number is defined as

$$R_e = \frac{R_2 u_2}{\nu} \tag{7.1}$$

where R_2 is the tip radius of the rotating shroud, ν is the kinematic viscosity of the fluid, $u_2 = \omega R_2$ is the tip speed of the rotating shroud. ν is a function of fluid temperature, which was kept almost constant ($\approx 62°$ F) during the experiment. So, the effect of the Reynolds number is actually the effect of the shaft speed.

F_n and F_t, measured using both the internal balance and the manometer, are presented in Figure 7.3. The magnitude of the radial force F due to the eccentric location of the rotating shroud is presented in Figure 7.4, and phase angle of F in Figure 7.5. It is seen that both normal and tangential forces, non-dimensionalized by $\frac{1}{2}\rho u_2^2 \varepsilon L$ (where ρ is the density of the fluid, u_2 the tip speed of the rotating shroud, ε eccentricity and L the projected length of the leakage path along meridional direction of the rotating shroud surface), are decreasing

as the shaft speed is increasing. This result is in constrast with Jery's result (1987) which indicates total hydrodynamic forces measured are not affected by the value of the Reynolds number. One of the reasons might be there is a rather big clearance between the front shroud of the impeller and the shroud of casing in Jery's experiment, so the viscous effect could be negligible. However, in the present experiment, since the clearance is very small, boundary layers on the surface of the shroud have a larger influence on the forces acting on the shroud.

7.3. Effect of Geometric Parameters

7.3.1 Effect of Width of Shroud Clearance

Measurements for three different clearances were performed while keeping a fixed eccentricity. Figures 7.8 to 7.10 show F_n, F_t, magnitude F and phase angle φ versus nondimensional clearance $H^* = H/R_2$ from 1.49×10^{-2} to 4.53×10^{-2}. It is seen that the forces increase very much as the width of clearance decreases. Notice also: as the clearance decreases, the ratio $\frac{F_t}{F_n}$ increases. Since F_t is the major possible destabilizing force, smaller shroud clearance may lead to an instability problem. Compare the ratio $\frac{F_t}{F_n}$ from this experiment ($\frac{F_t}{F_n} = 1.1$ to 1.7) and Adkins experiment ($\frac{F_t}{F_n} \approx 0.25$), one can see for larger clearance $\frac{F_t}{F_n}$ is much smaller.

7.3.2. Effect of Eccentricity

Eccentricity is the most important geometric parameter because it drives the hydrodynamic forces acting on the shroud. Measurements for three different eccentricities were performed while keeping a fixed width of shroud clearance.

Figures 7.11 to 7.13 show F_n, F_t, magnitude F and phase angle φ versus $\varepsilon^* = \varepsilon/H$ from 0.228 to 0.898 ($H = 0.167$ in.). Examination of the graphs shows that the radial forces, already nondimensionalized by $\frac{1}{2}\rho u_2^2 \varepsilon L$, still increases as square root of ε^*. This finding would mean that F_n and F_t are approximately functions of ε^* to the power of $3/2$.

7.3.3. Effect of Face Seal Clearance

Measurements were performed for the face seal clearance $\delta = 0.020$ in. and 0.185 in. The rest of the test conditions was the same. The result was represented in Figure 7.9. It shows the larger seal clearance results in smaller force on the shroud. The reason is the larger seal clearance allows a larger flow rate and smaller pressure rise across the shroud. This might influence the pressure distributions around the shroud.

7.4. Steady Pressure Distributions

The static head coefficients $\psi = \frac{p_2 - p_1}{\frac{1}{2}\rho u_2^2}$ plotted against the shaft speeds (Fig. 7.14) indicates that the shroud force measurement apparatus behaves like a pump.

In Figure 7.15, a typical pressure distribution curve along the circumferential direction of the rotating shroud was presented. The experimental results show the circumferential pressure distribution curves are of modified sinusoidal shape, which is similar to the pressure distrubution in a journal bearing.

Figure 7.16 shows the pressure distributions along the meridional direction of the rotating shroud. This information will be useful to compare with any

theoretical solutions in the future.

7.5. Dynamic Pressure Measurements

Since no whirl motion was performed in this experiment, the magnitude of the pressure fluctuations are small, about five percent of the pressure difference between the inlet and outlet of the leakage path. The magnitude of pressure fluctuation was defined as peak to peak value of the ensemble averaged data. Figure 7.17 shows the magnitude of the pressure fluctuations as functions of clearance geometry and shaft speed. It is seen from the graph that they are not proportional to the square of the shaft speeds.

Figures 7.18 to 7.19 show the ensemble averaged data and spectra for some typical unsteady pressure measurements. The noise in 60 Hz and 300 Hz was from the electrical system. Interestingly, in many measurements, the biggest magnitude of Fourier coefficient corresponded to one quarter or half of the shaft frequency. This phenomenon might have some similarity with disc friction flow. Stafford, et al (1975) reported an experimental investigation about a disc rotating between stationary side walls and discharging fluid into a reservoir. It was found when the disc diameter was made smaller than walls, the flow became unsteady. Further reduced disc/wall diameter ratio produced a pulsating flow. The pulse frequency was in a range of $\frac{1}{10}$ to $\frac{1}{2}$ of shaft frequency for different geometry. However, since the sampling frequency used in the present experiment was high, there are only three frequencies below the shaft frequency in the spectrum. Detailed comments for present measurements could not be made.

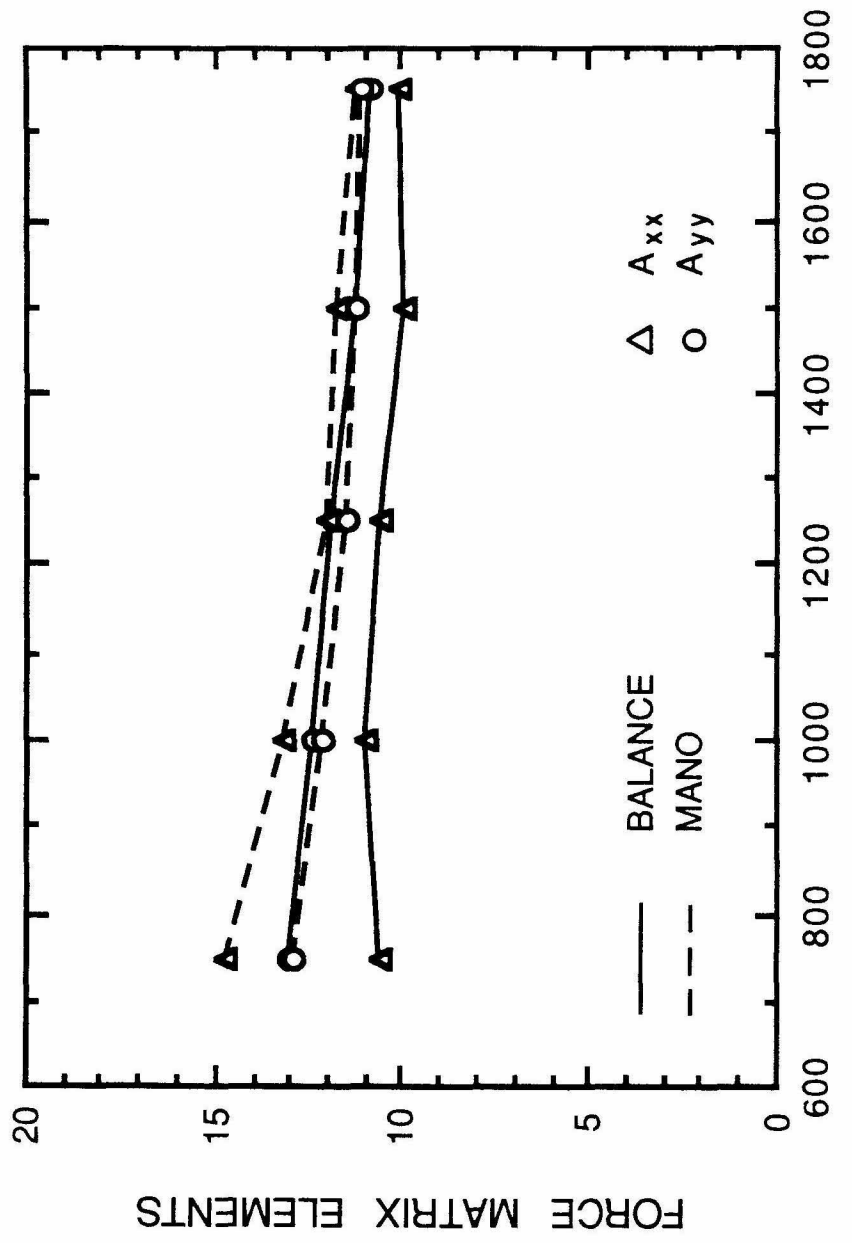

Fig. 7.1 The dimensionless diagonal elements of the hydrodynamic force matrix, $[A]$, as a function of the shaft speed, with $\varepsilon = 0.150$ in, $\delta = 0.020$ in, and $H = 0.167$ in.

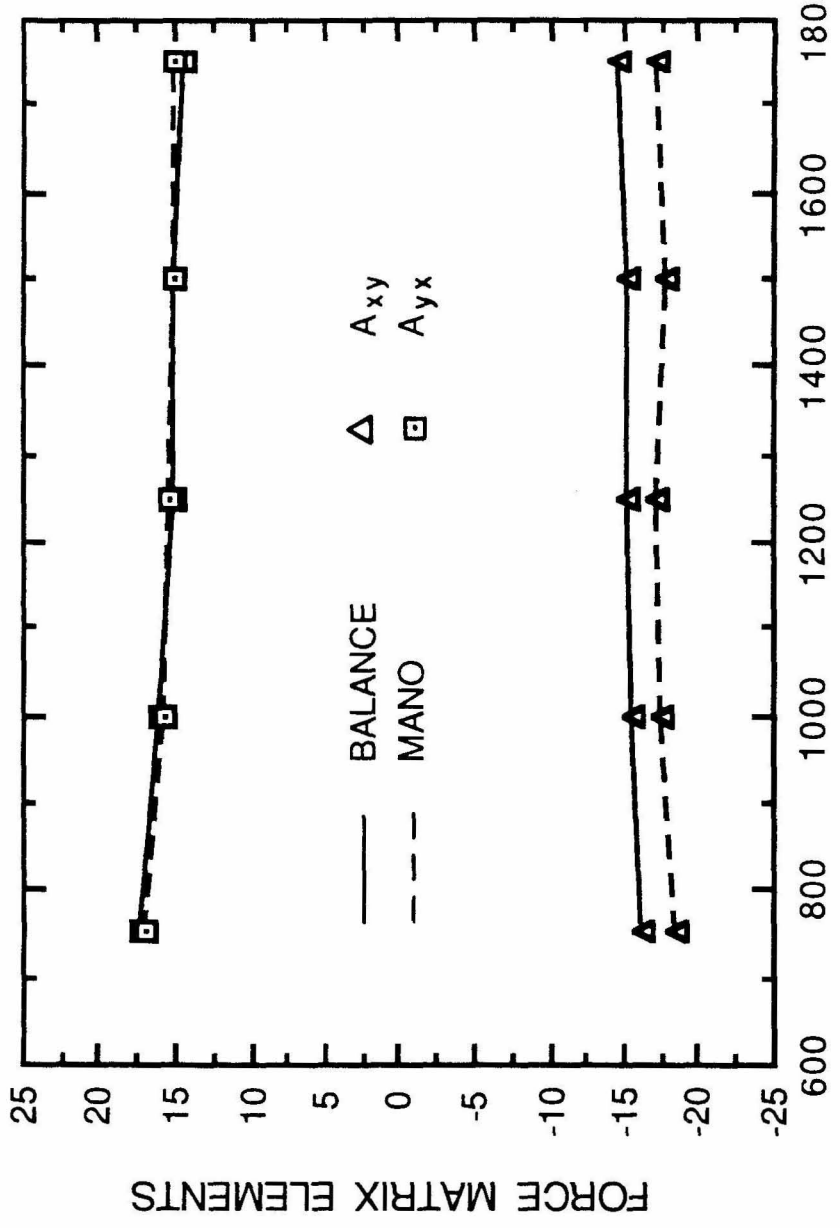

Fig. 7.2 The dimensionless off-diagonal elements of the hydrodynamic force matrix, $[A]$, as a function of the shaft speed, with $\epsilon = 0.150$ in, $\delta = 0.020$ in, and $H = 0.167$ in.

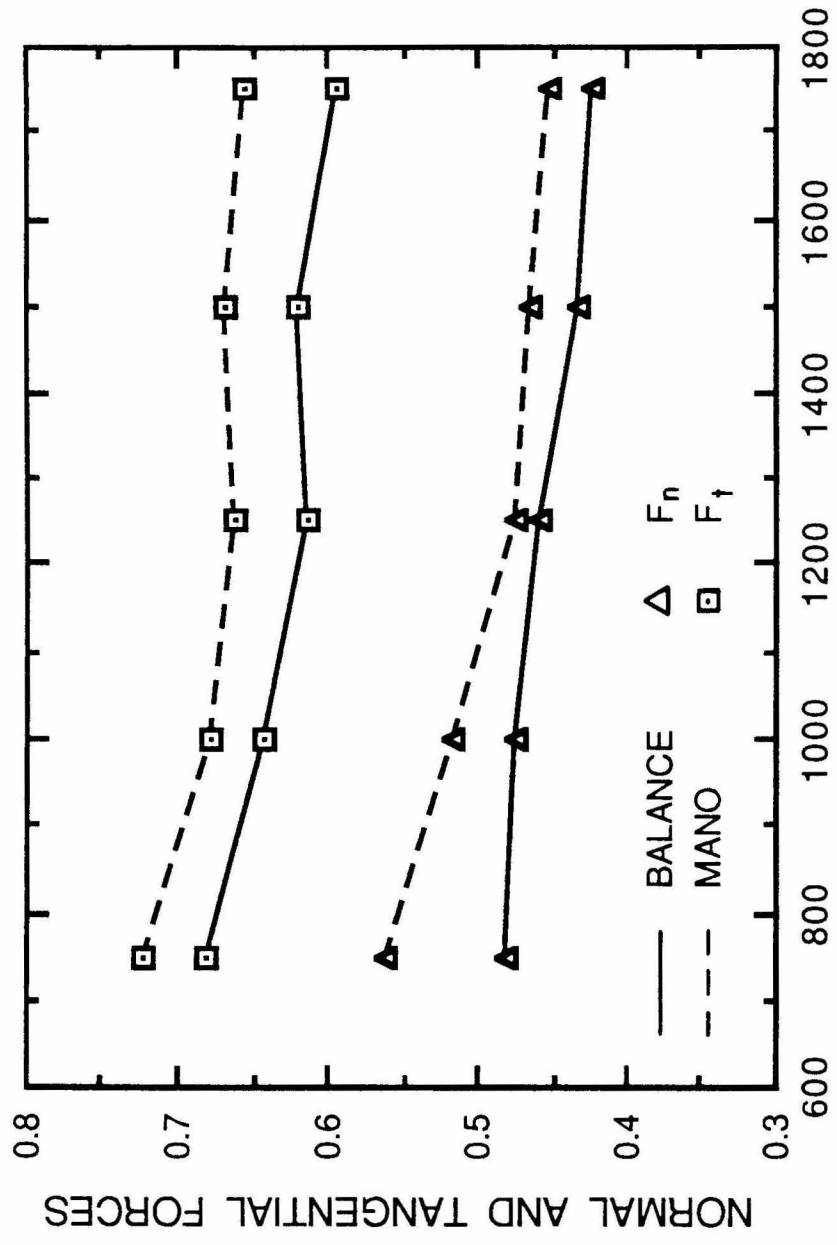

Fig. 7.3 The dimensionless normal and tangential components of the shroud lateral hydrodynamic force, F_n and F_t as a function of the shaft speed, with $\varepsilon = 0.150$ in, $\delta = 0.020$ in, and $H = 0.167$ in.

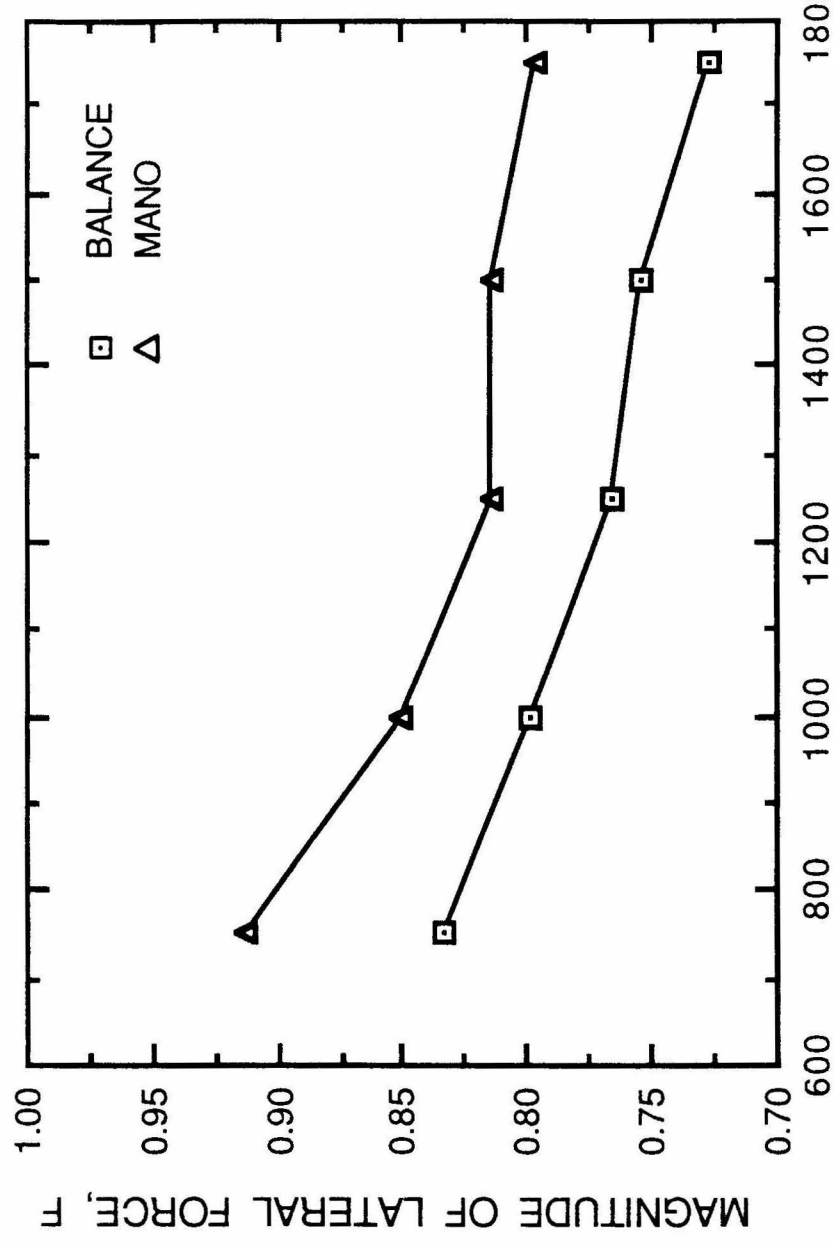

Fig. 7.4 The dimensionless magnitude of the shroud lateral hydrodynamic force, F, due to the eccentric position of the rotating shroud, as a function of the shaft speed, with $\varepsilon = 0.150$ in, $\delta = 0.020$ in, and $H = 0.167$ in.

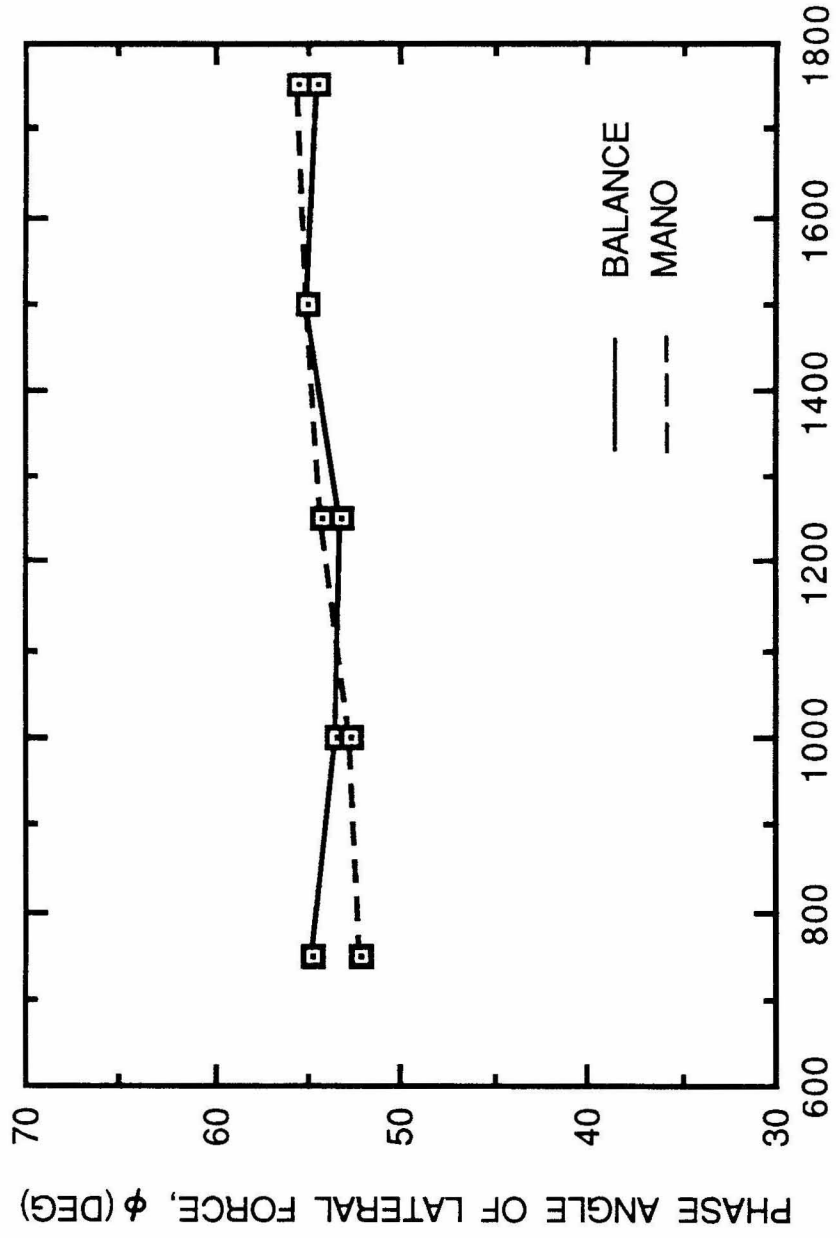

Fig. 7.5 The phase angles of the shroud lateral hydrodynamic forces, F, due to the eccentric position of the rotating shroud as a function of the shaft speed with $\varepsilon = 0.150$ in, $\delta = 0.020$ in, and $H = 0.167$ in.

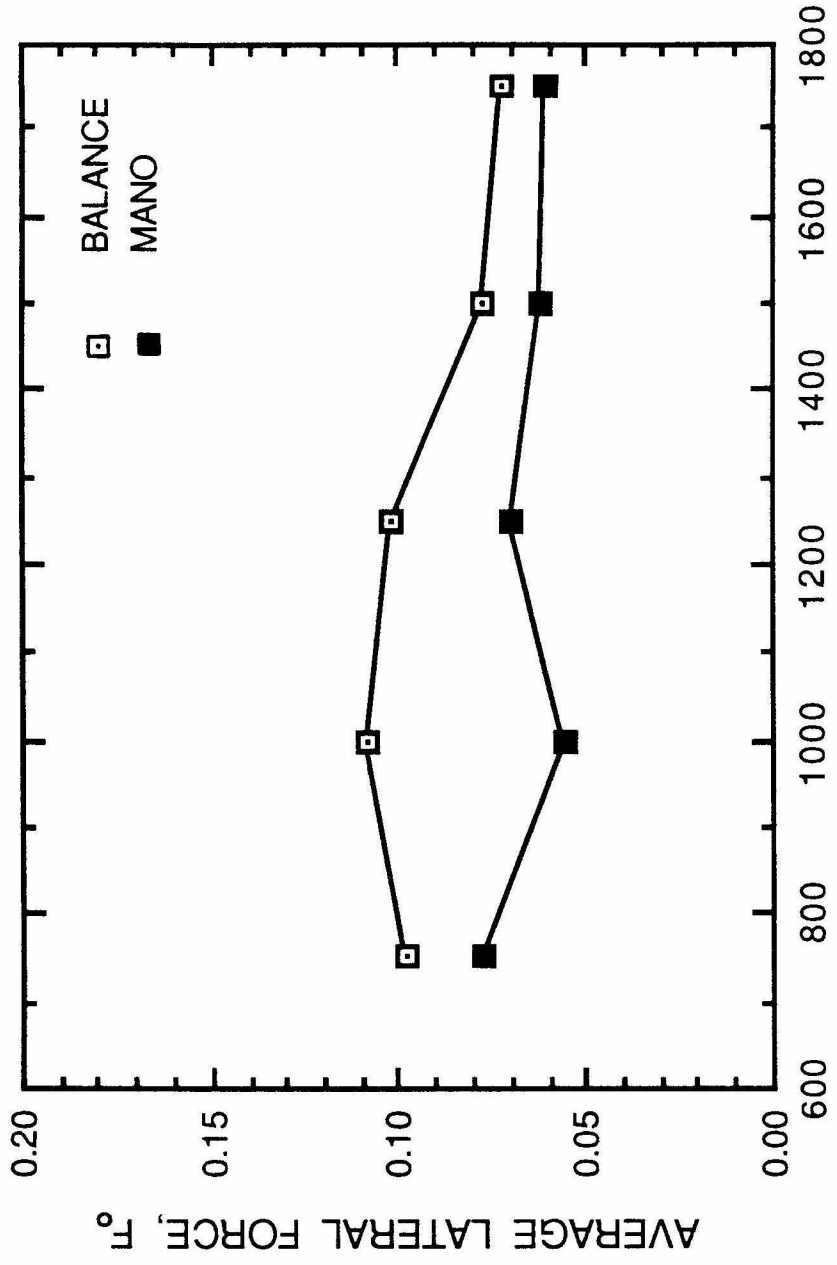

Fig. 7.6 The dimensionless average shroud lateral hydrodynamic force, F_o, as a function of the shaft speed, with $\varepsilon = 0.150$ in, $\delta = 0.020$ in, and $H = 0.167$ in.

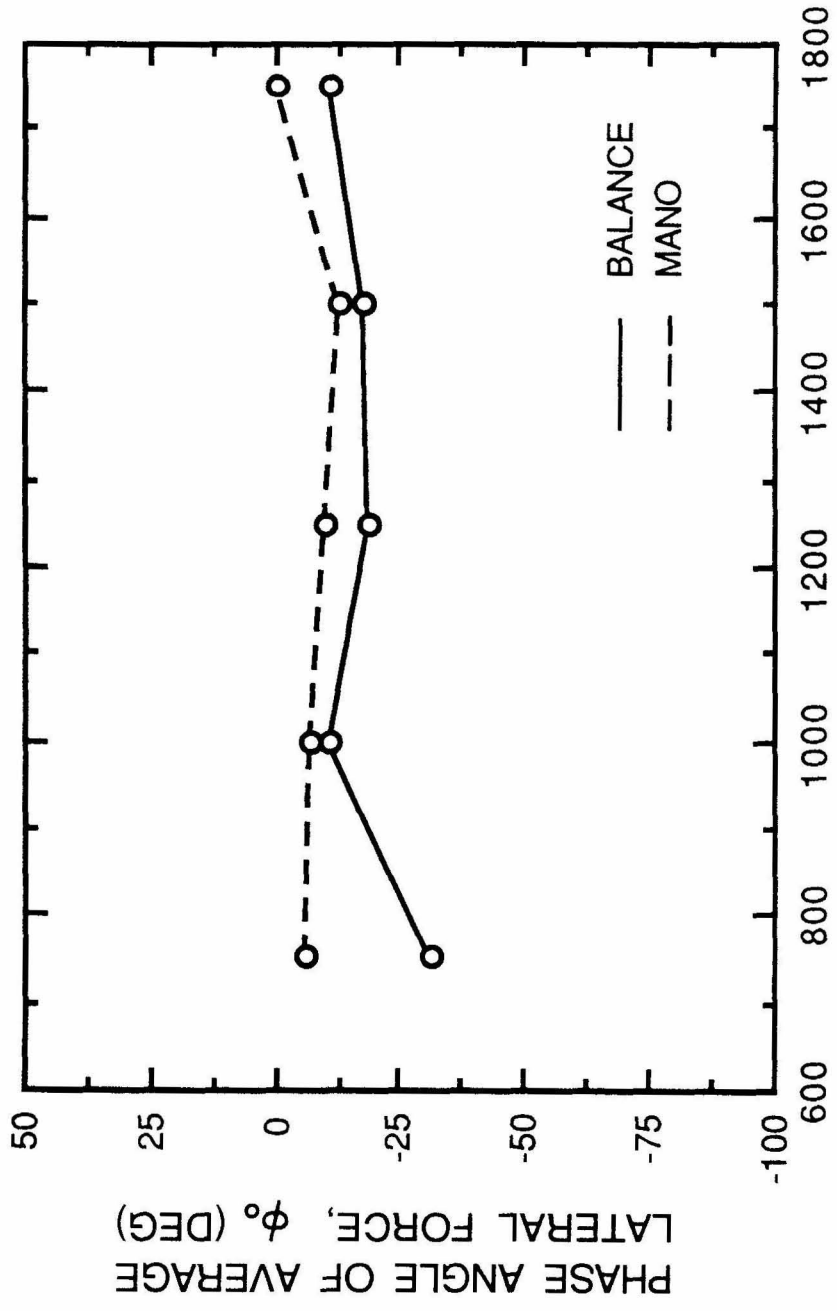

Fig. 7.7 The phase angles of the average shroud lateral hydrodynamic force, φ_o, as a function of the shaft speed, with $\varepsilon = 0.150$ in, $\delta = 0.020$ in, and $H = 0.167$ in.

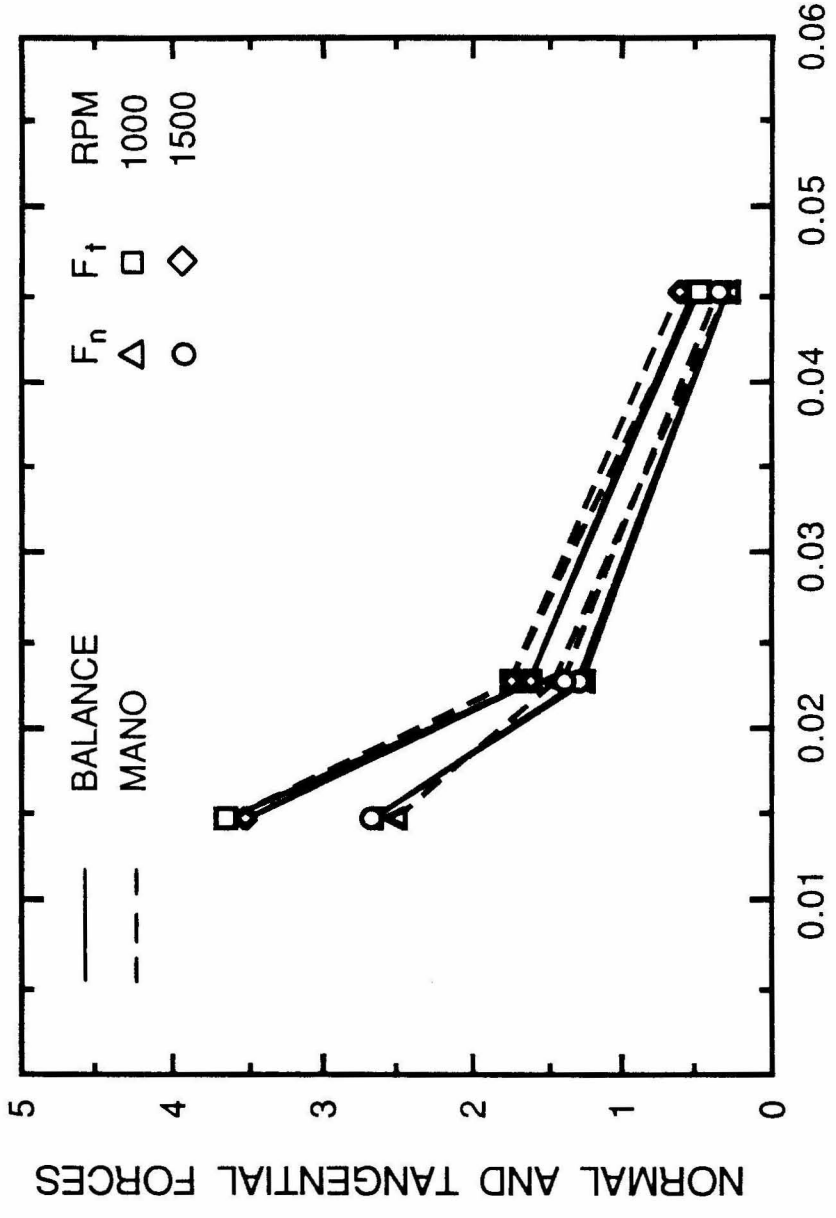

Fig. 7.8 The dimensionless normal and tangential components of the shroud lateral hydrodynamic force, F_n and F_t, as a function of the dimensionless shroud clearance, H^*, with $\varepsilon = 0.038$ in, $\delta = 0.020$ in.

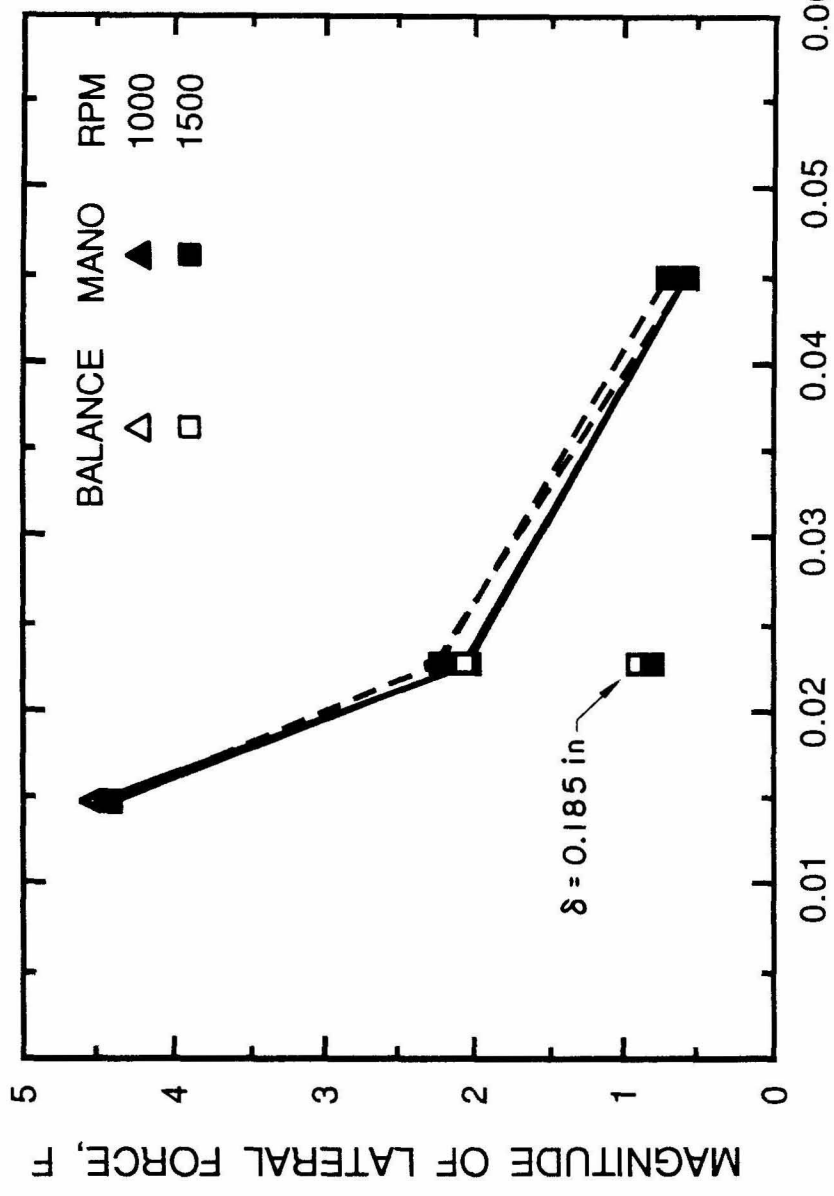

Fig. 7.9 The dimensionless magnitude of the shroud lateral hydrodynamic force, F, due to the eccentric position of the rotating shroud, as a function of the dimensionless shroud clearance, H^*, with $\varepsilon = 0.038$ in, $\delta = 0.020$ in. The figure also shows the magnitude of the force for $\delta = 0.185$ in.

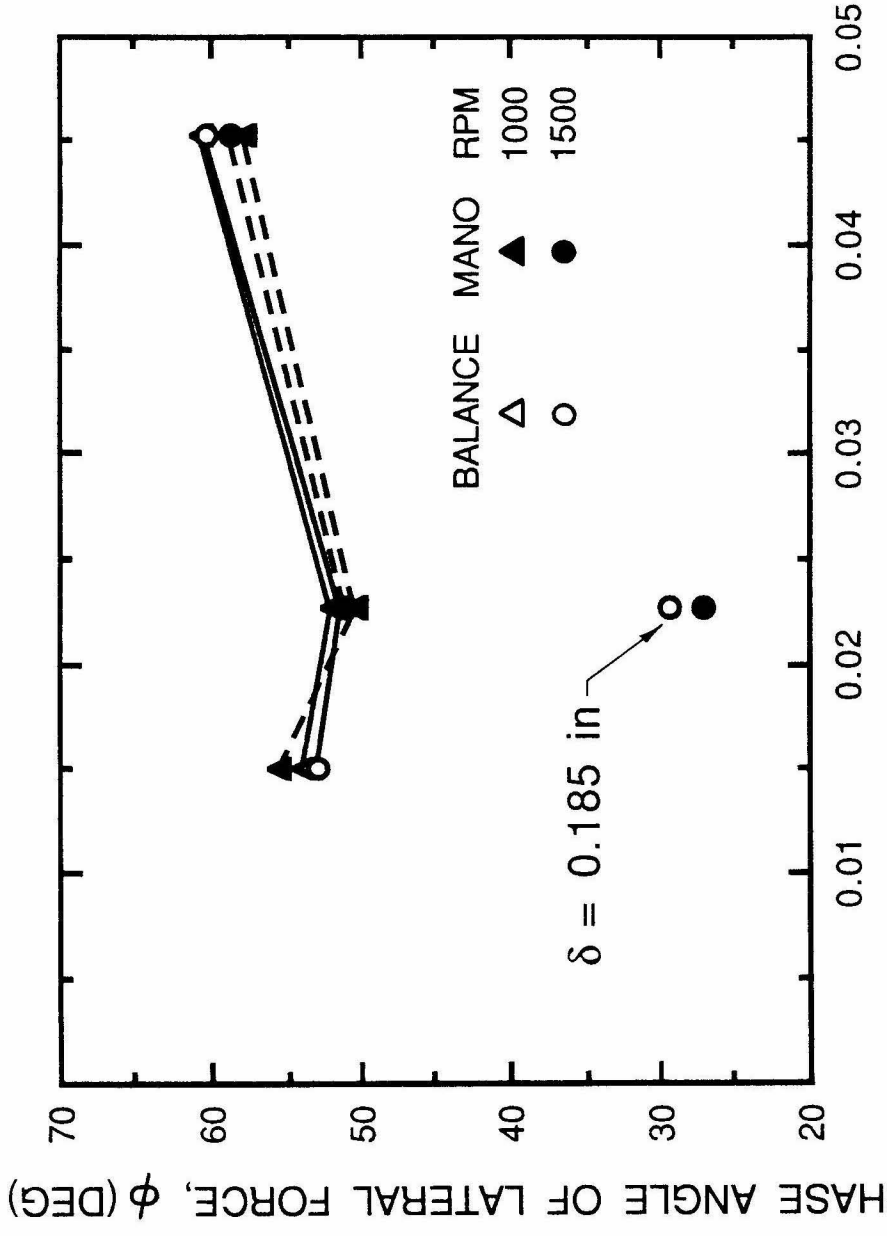

Fig. 7.10 The phase angles of the shroud lateral hydrodynamic forces, F, due to the eccentric position of the rotating shroud, as a function of the dimensionless shroud clearance H^*, with $\varepsilon = 0.038$ in, $\delta = 0.020$ in. The figure also shows the phase angle of the force for $\delta = 0.185$ in.

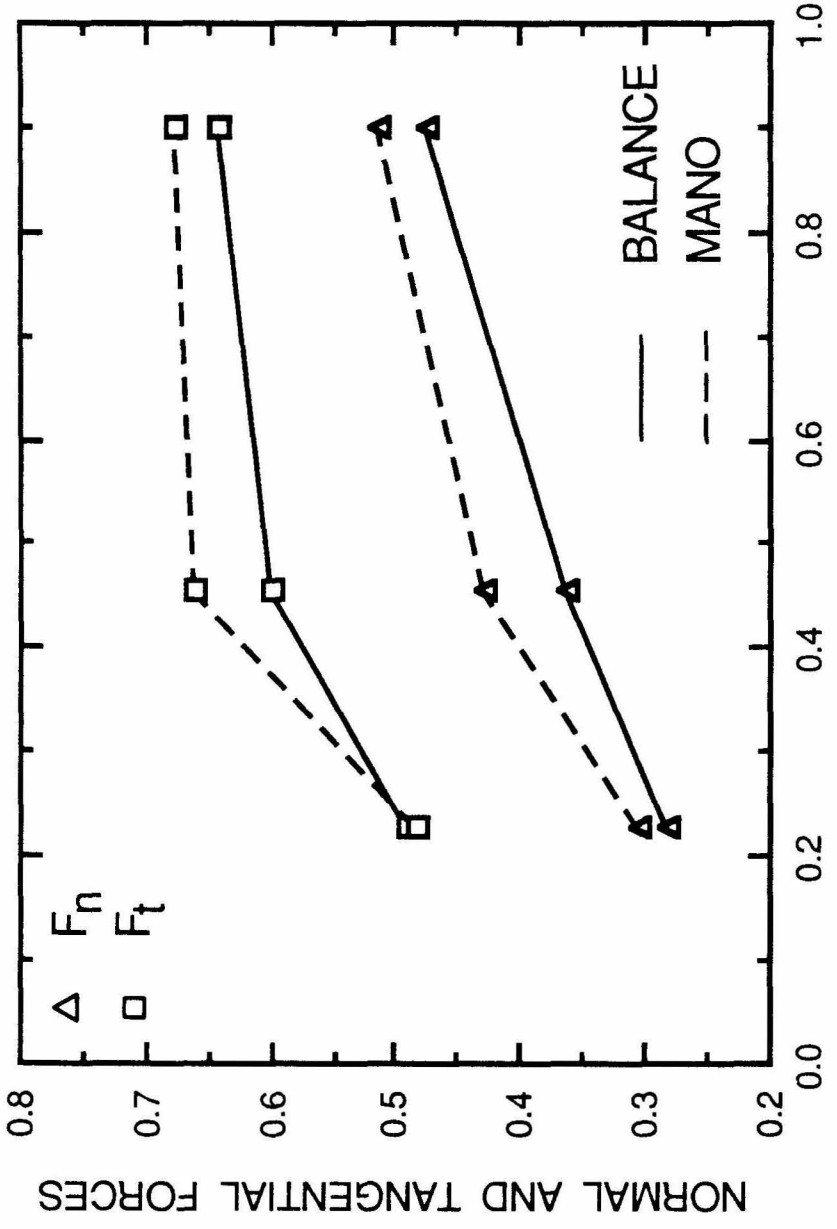

Fig. 7.11 The dimensionless normal and tangential components of the shroud lateral hydrodynamic force, F_n and F_t, as a function of the dimensionless eccentricity, ϵ^*, with $H = 0.167$ in, and $\delta = 0.020$ in.

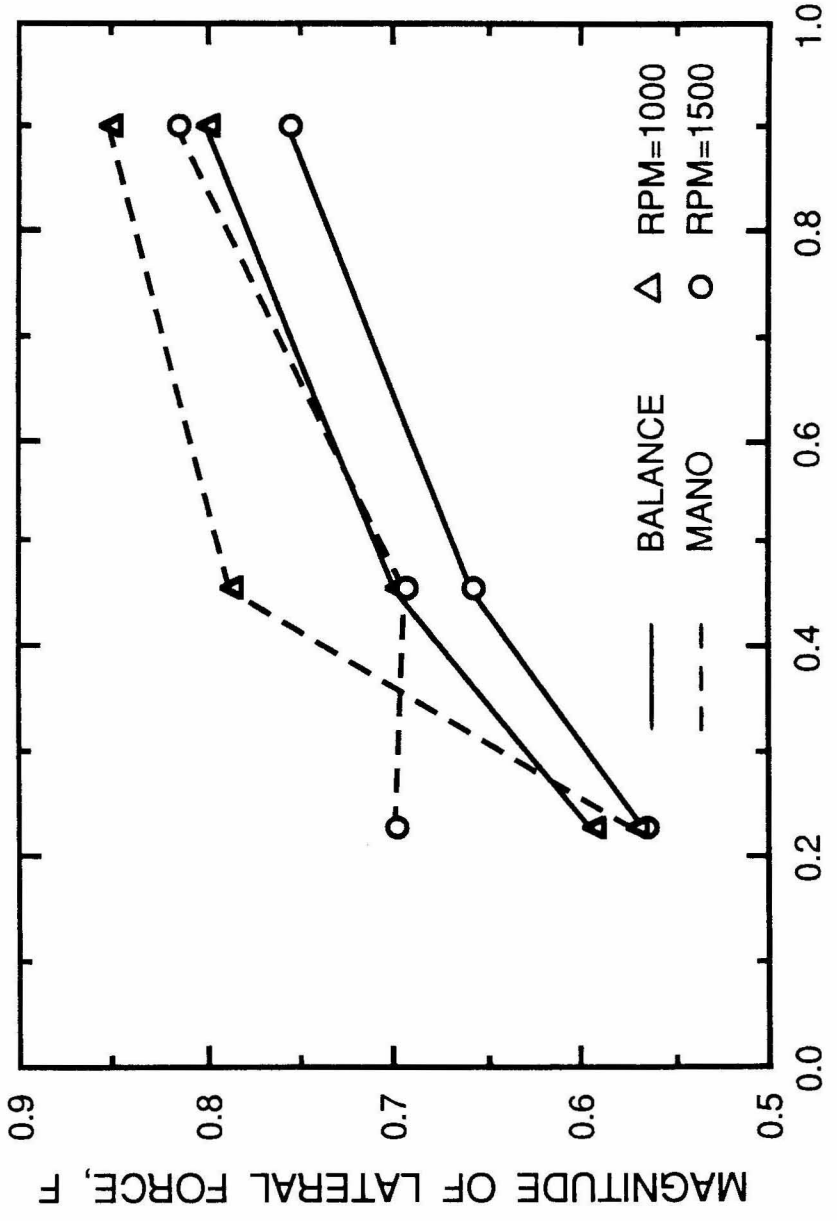

Fig. 7.12 The dimensionless magnitude of the shroud lateral hydrodynamic force, F, due to the eccentric position of the rotating shroud, as a function of the dimensionless eccentricity, ϵ^*, with $H = 0.167$ in, and $\delta = 0.020$ in.

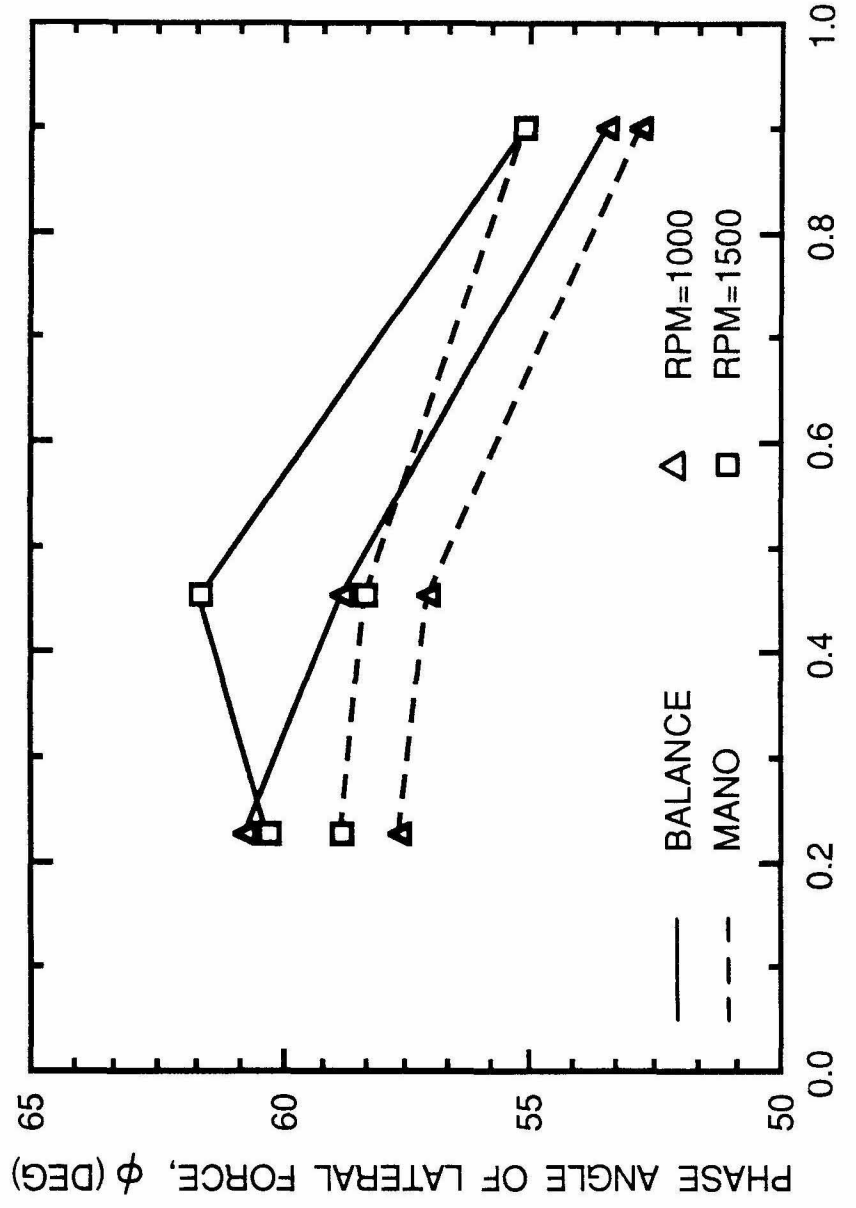

Fig. 7.13 The phase angles of the shroud lateral hydrodynamic force as a function of the dimensionless eccentricity ε^*, with $H = 0.167$ in, and $\delta = 0.020$ in.

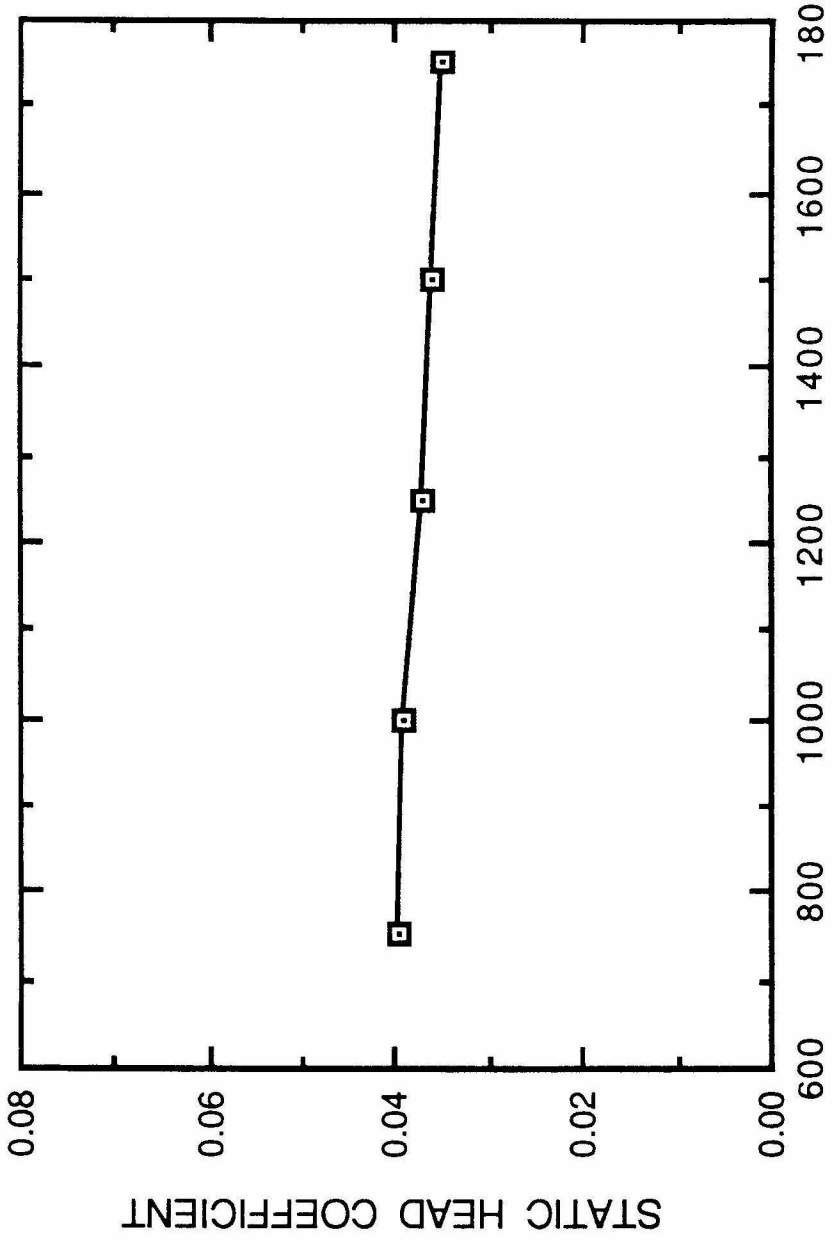

Fig. 7.14 The static head coefficient, averaged over four eccentric positions, as a function of the shaft speed, with $\epsilon = 0.150$ in, $\delta = 0.020$ in, and $H = 0.167$ in.

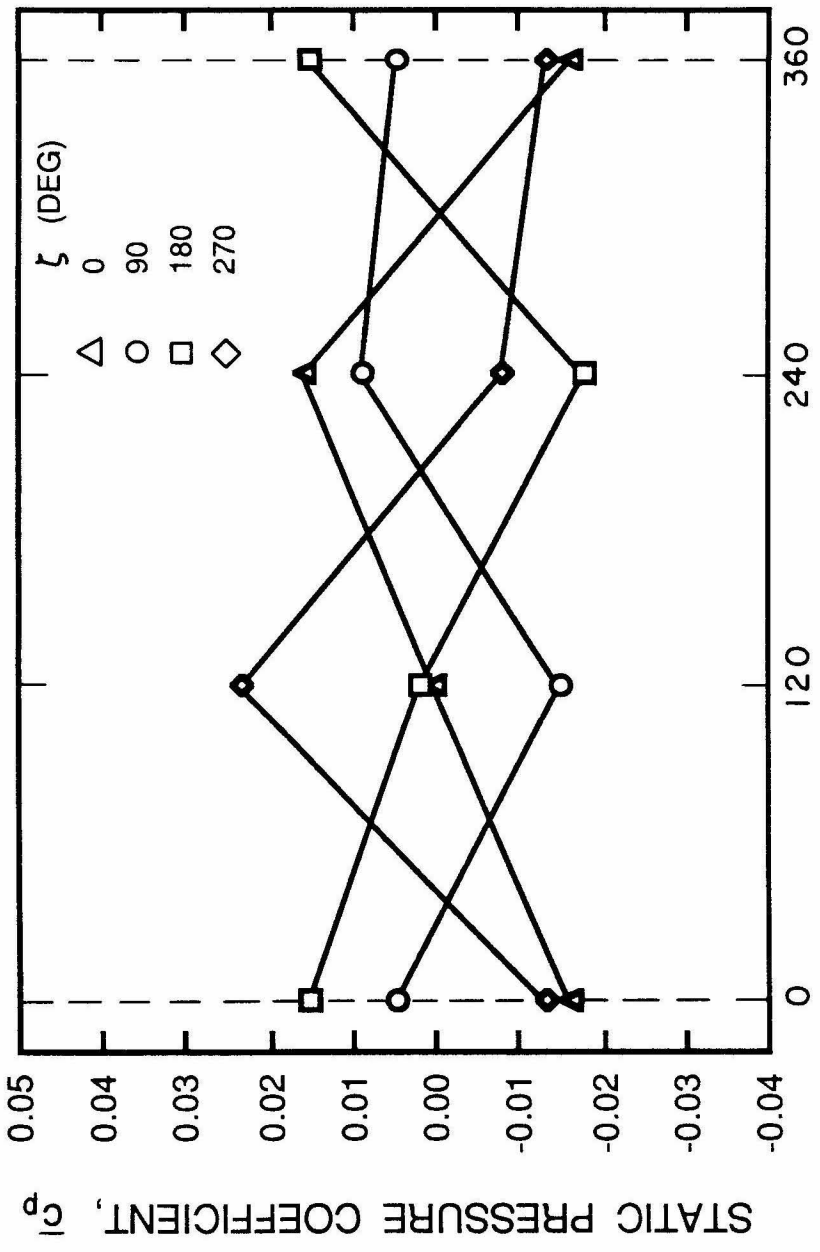

Fig. 7.15 Some typical dimensionless steady pressure distributions at outlet area along the circumferential directions of the rotating shroud surface, with $\varepsilon = 0.150$ in, $\delta = 0.020$ in, $H = 0.167$ in, and RPM=1000.

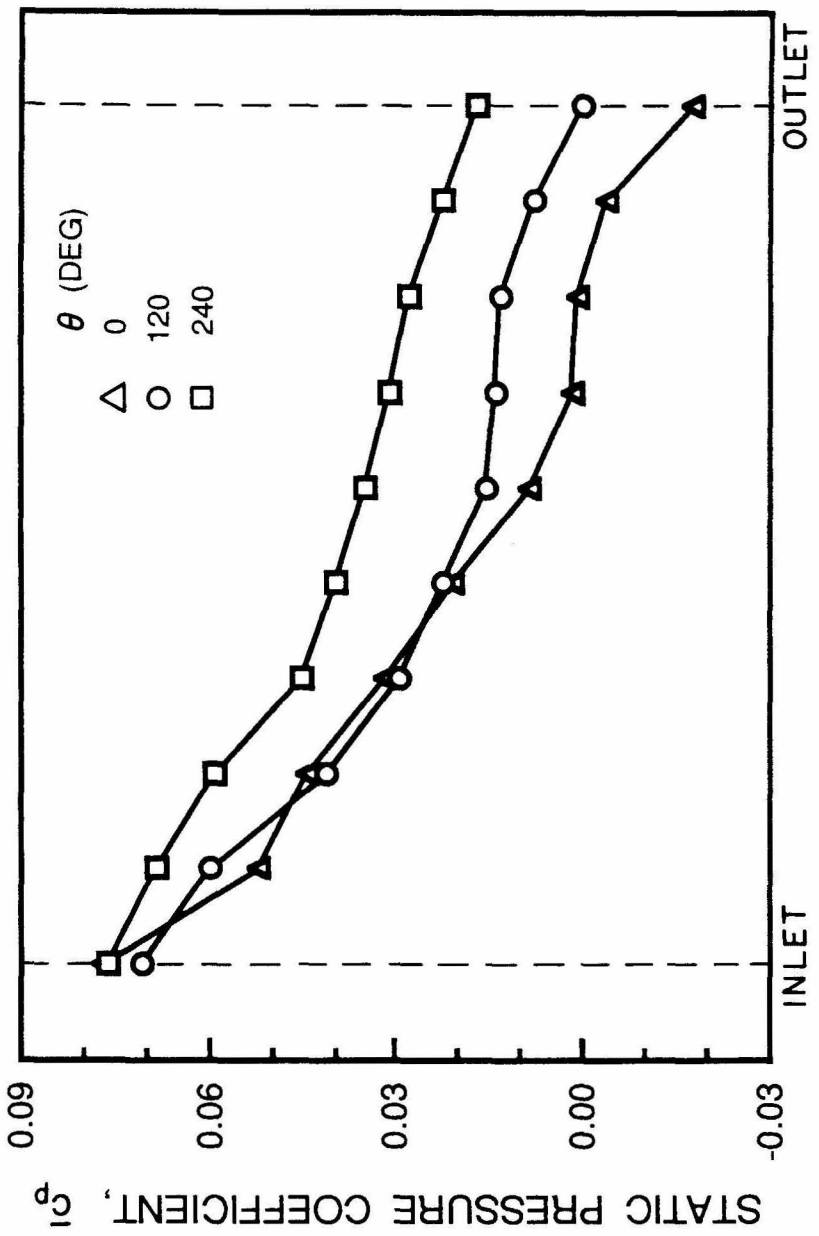

Fig. 7.16 Some typical dimensionless steady pressure distributions along the meridional direction of the rotating shroud surface, with $\varepsilon = 0.038$ in, $\delta = 0.020$ in, $H = 0.084$ in, $\varsigma = 0°$, and RPM=1000.

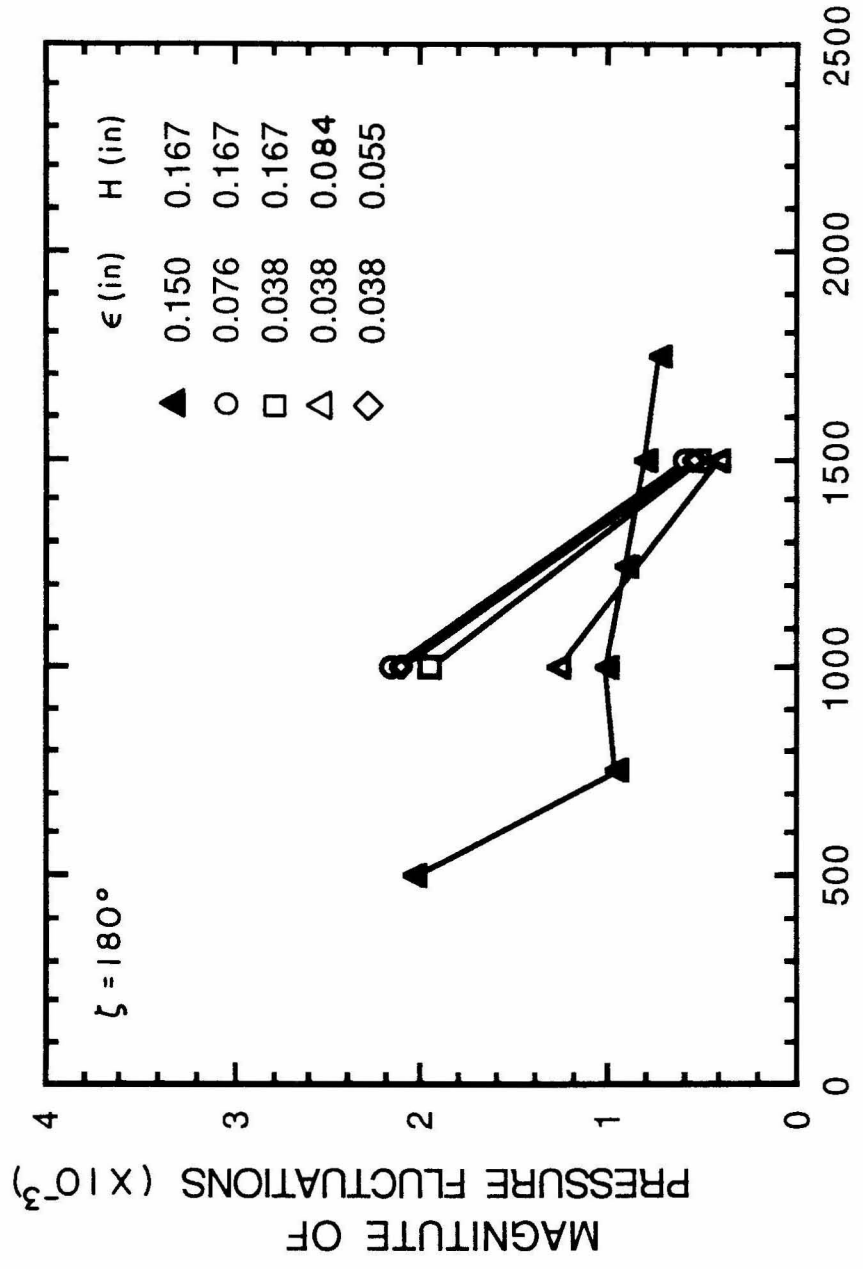

Fig. 7.17 The dimensionless magnitude of the unsteady pressure fluctuations as functions of the clearance geometry and shaft speed.

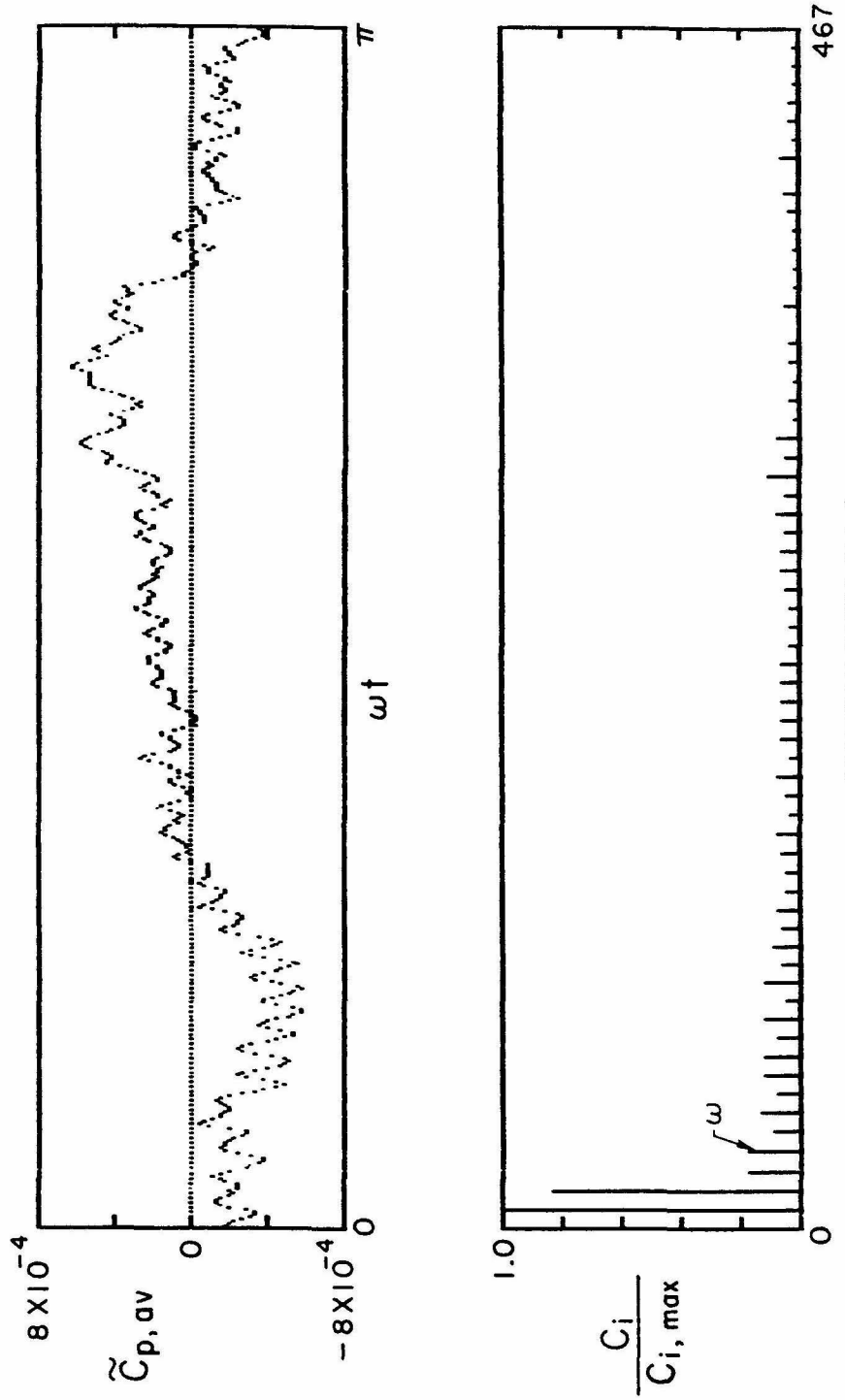

Fig. 7.18 Spectrum of unsteady pressure measurements and ensemble averaged unsteady pressure measurements (RPM = 1750, $\varepsilon = 0.150$ in, $\delta = 0.020$ in, $H = 0.167$ in, and $\zeta = 90°$).

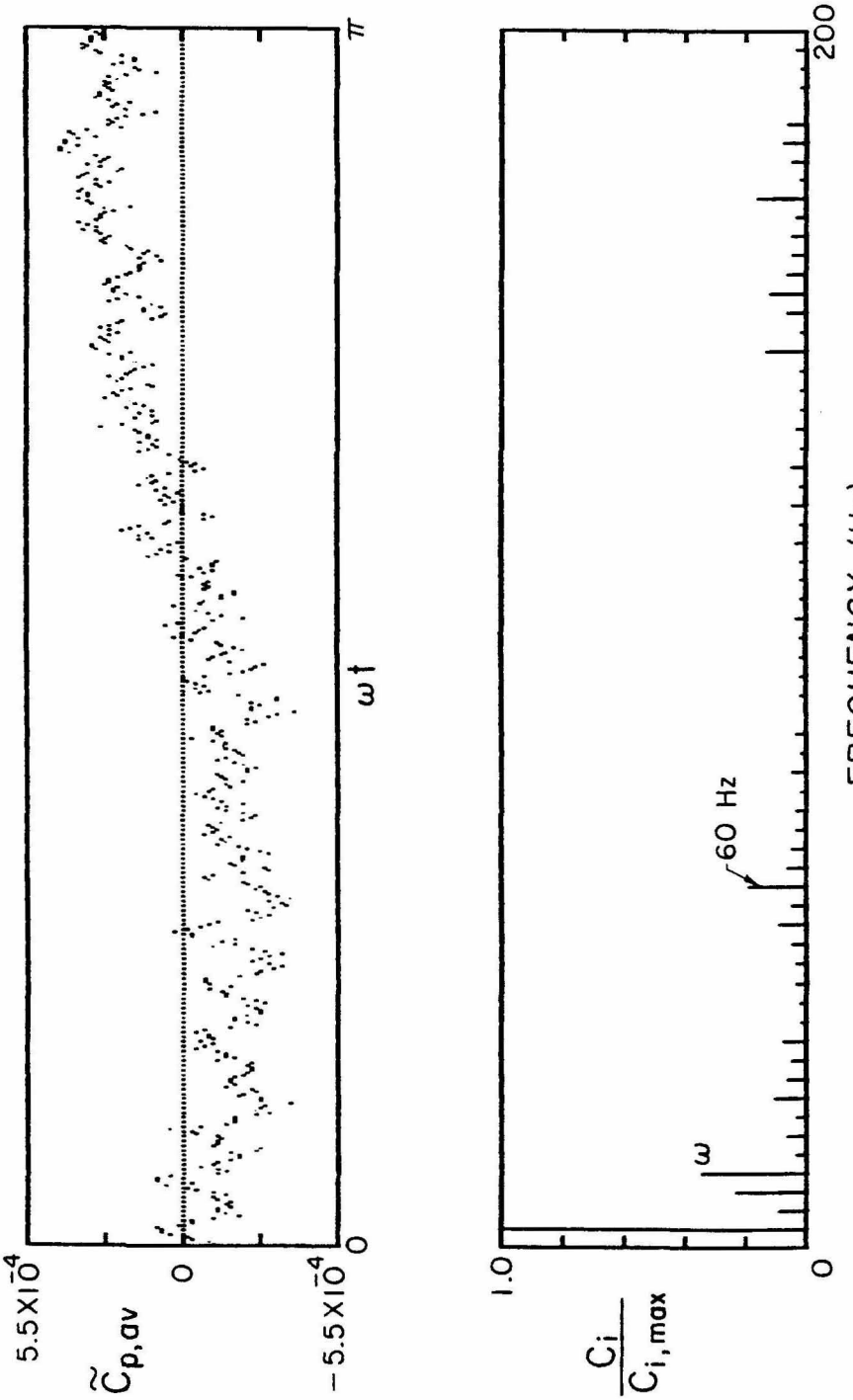

Fig. 7.19 Spectrum of unsteady pressure measurements and ensemble averaged unsteady pressure measurements ($RPM = 750$, $\varepsilon = 0.150$ in, $\delta = 0.020$ in, $H = 0.167$ in, and $\varsigma = 180°$).

Chapter 8

SUMMARY AND CONCLUSION

Based on the need to understand the impeller shroud forces, an experimental apparatus was designed to simulate the impeller shroud leakage flow. Hydrodynamic forces, steady and dynamic pressure distributions on the rotating shroud were measured as functions of eccentricity, width of shroud clearance, seal clearance and shaft rotating speed. From these measurements, the following can be concluded:

1) The hydrodynamic force matrix $[A]$ in this experiment is statically unstable. The diagonal terms are equal in magnitude and have the same positive sign, resulting in a radially outward fluid force F_n. The off-diagonal terms are equal in magnitude and their opposite signs are such as to produce a tangential fluid force, F_t, encouraging forward whirl motion of the rotating shroud. These findings are qualitatively similar to the hydrodynamic volute force of a complete pump.

2) Both non-dimensionalized normal and tangential hydrodynamic forces acting on the rotating shroud decrease as Reynolds number increases. This effect is a function of the shroud clearance.

3) The hydrodynamic forces acting on the rotating shroud are a strong nonlinear function of the eccentricity as the $\frac{3}{2}$ power.

4) For a fixed eccentricity, reducing clearance substantially increases F_n and F_t. The forces vary approximately inversely with $\frac{3}{2}$ power of this clearance. The ratio F_t/F_n is also a function of this clearance.

5) The forces decrease and the ratio F_t/F_n decreases when the front face seal opening is increased. It was observed that the local pressures are relieved by this opening. It is also possible that the shroud leakage flow rate is changed but the effect of this leakage on forces is unknown.

6) The sub-harmonic frequency pressure fluctuations were observed which may affect adversely the behavior of the rotor system.

This experiment is the first step of an on-going shroud force test program.

References

Adkins, D. R., 1986, "Analyses of Hydrodynamic Forces on Centrifugal Pump Impellers," Ph.D. Thesis, Division of Engineering and Applied Science, California Institute of Technology, Pasadena, CA.

Adkins, D. R. and Brennen, C. E., 1988, "Analyses of Hydrodynamic Radial Forces on Centrifugal Pump Impellers," ASME *Journal of Fluids Engineering*, **110**(1), 20-28.

Arndt, N., 1988, "Experimental Investigation of Rotor-Stator Interaction in Diffuser Pumps," Ph.D. Thesis, Division of Engineering and Applied Science, California Institute of Technology, Pasadena, CA.

Bolleter, U., Wyss, A., Welte, I., and Stürchler, R., 1987, "Measurement of Hydrodynamic Interaction Matrices of Boiler Feed Pump Impellers," ASME *Journal of Vibration, Acoustics, Stress, and Reliability in Design*, **109**(2), 144-151.

Braisted, D. M., 1979, "Cavitation Induced Instabilities Associated with Turbomachines," Ph.D. Thesis, Division of Engineering and Applied Science, California Institute of Technology, Pasadena, CA.

Brennen, C. E., 1976, "On the flow in an annulus surrounding a whirling cylinder," *J. Fluid Mech.* **75**(1), 173-191.

Brennen, C. E., Acosta, A. J., and Caughey, T. K., 1980, "A Test Program to Measure Fluid Mechanical Whirl-Excitation Forces in Centrifugal Pumps," Proceedings of the First Workshop on Rotordynamic Instability Problems in High-Performance Turbomachinery, Texas A&M University, College Station, Texas, NASA CP 2133, pp. 229-235.

Chamieh, D. S., 1983, "Forces on a Whirling Centrifugal Pump-Impeller," Ph.D. Thesis, Division of Engineering and Applied Science, California Institute of Technology, Pasadena, CA.

Chamieh, D. S., Acosta, A. J., Brennen, C. E., and Caughey, T. K., 1985, "Experimental Measurements of Hydrodynamic Radial Forces and Stiffness Matrices for a Centrifugal Pump-Impeller," ASME *Journal of Fluids Engineering*, **107**(3), 307-315.

Childs, D. W., 1983, "Finite Length Solutions for Rotordynamic Coefficients of Turbulent Annular Seals," ASME *J. of Lubrication Technology*, **105**, 437-444.

Childs, D. W., 1986, "Force and Moment Rotordynamic Coefficients for Pump-Impeller Shroud Surfaces," Proceedings of the Fourth Workshop on Rotordynamic Instability Problems in High-Performance Turbomachinery, Texas A&M University, College Station, Texas, NASA CP 2443, pp. 503-529.

Childs, D. W., 1987, "Fluid-Structure Interaction Forces at Pump-Impeller-Shroud Surfaces for Rotordynamic Calculations," Proceedings of the ASME Vibration Conference, Boston, MA.

Franz, R., 1989, "Experimental Investigation of the Effect of Cavitation on the Rotordynamic Forces on a Whirling Centrifugal Pump Impeller," Ph.D. Thesis, Division of Engineering and Applied Science, California Institute of Technology, Pasadena, CA.

Franz, R. and Arndt, N., 1986, "Measurements of Hydrodynamic Forces on a Two-Dimensional Impeller and a Modified Centrifugal Pump," Division of Engineering and Applied Science, California Institute of Technology, Pasadena, CA, Report No. E249.4.

Franz, R., Arndt, N., Caughey, T. K., Brennen, C. E., and Acosta, A. J., 1987, "Rotordynamic Forces on Centrifugal Pump Impellers," Proceedings of the Eighth Conference on Fluid Machinery, Akadémiai Kiadó, Budapest, Hungary, Vol. 1, pp. 252-258.

Hergt, P. and Krieger, P., 1969-70, "Radial Forces in Centrifugal Pumps with Guide Vanes," *Advance Class Boiler Feed Pumps, Proceedings of the Institute of Mechanical Engineers*, **184**(3N), 101-107.

Jery, B., Brennen, C. E., Caughey, T. K., and Acosta, A. J., 1985, "Forces on Centrifugal Pump Impellers," Second International Pump Symposium, Houston, TX.

Jery, B., 1987, "Experimental Study of Unsteady Hydrodynamic Force Matrices on Whirling Centrifugal Pump Impellers," Ph.D. Thesis, Division of Engineering and Applied Science, California Institute of Technology, Pasadena, CA.

Kanki, H., Kawata, Y., and Kawakami, T., 1981, "Experimental Research on the Hydraulic Excitation Force on the Pump Shaft," ASME Paper No. 81-DET-71.

Ng, S. L., 1976, "Dynamic Response of Cavitating Turbomachines," Ph.D. Thesis, Division of Engineering and Applied Science, California Institute of Technology, Pasadena, CA.

Ohashi, H., Shoji, H., 1987, "Lateral Fluid Forces on a Whirling Centrifugal Impeller (2nd Report: Experiment in Vaneliss Diffuser)," ASME *Journal of Fluids Engineering*, **109**(2), 100-106.

Sherzer, A. F., 1924, "Determination of Internal Leakage in Centrifugal Pumps," *Engineering News-Record*, **92**, No. 25, 1056-1058.

Stafford, J. A. T., Ferguson, T. B., Hirst, E. S. and Asquith, R. W., 1975, "An Experimental Investigation Observing Some Unsteady Flows Induced by a Rotating Disc," *Proc. of the 5th Conference on Fluid Machinery*, **2**, 1071-1079, Budapest.

Stepanoff, A. J., 1932, "Leakage Loss and Axial Thrust in Centrifugal Pumps," *Trans. ASME*, 65-111.